Metal Abundances in the Hot Interstellar Medium in Early-Type Galaxies Observed with ASCA

Kyoko Matsushita, Takaya Ohashi

Department of Physics, Tokyo Metropolitan University, 1-1 Minami-Ohsawa Hachioji, Tokyo 192-03

matusita@phys.metro-u.ac.jp

and

Kazuo Makishima

Department of Physics, University of Tokyo, 7-3-1 Hongo, Bunkyo-ku, Tokyo 113

Research Center for the Early Universe (RESCEU), University of Tokyo, 7-3-1 Hongo, Bunkyo-ku, Tokyo 113

Abstract

We have analyzed ASCA data of 27 early-type galaxies, and studied the properties of their X-ray emitting ISM (Inter Stellar Medium) in detail. We found that overlapping lines and free-bound continuum cause strong coupling in the derived abundances of various elements. The abundance determination is also difficult due to the uncertainties in the Fe-L atomic physics, because Fe-L lines couple with O and Ne K-lines. However, when abundances of α-elements are fixed, all the plasma codes give similar Fe abundances with a scattering of only 20–30%. To relax the strong coupling among the elements, we included 20% systematic errors in the Fe-L region of the spectra. Then, in X-ray luminous galaxies, the derived abundance of Fe and α-elements both became ~ 1 solar within a factor of 2. This result relaxes the previous severe discrepancy between the ISM and stellar metallicities. The ISM metallicity in X-ray fainter galaxies is still uncertain, but we can at least constrain that contribution from type-Ia SN to the ISM abundance is lower than in X-ray luminous systems. These results strongly suggest that a large fraction of SN Ia products have escaped into intergalactic space.

1. Introduction

Discovery of X-ray emitting hot Interstellar Medium (ISM) with the *Einstein observatory* has drastically renewed the view of early-type galaxies (Forman et al. 1985; Trinchieri et al. 1986; Canizares et al. 1987; Fabbiano et al. 1988; Fabbiano 1989). Since the hot ISM is considered to be gravitationally confined to a galaxy, X-ray observations provide useful knowledge about the depth and the shape of gravitational potential. Furthermore, chemical composition of the ISM tells us about the past history of the galaxy evolution, since stellar mass-loss products and supernova ejecta are accumulated in the ISM.

The ISM is metal-enriched by stellar mass loss and Type Ia SNe that are currently observed in elliptical galaxies. The standard supernova rates predict the metallicity of ISM to be as high as several times the solar value (e.g. Loewenstein and Mathews 1991; Ciotti et al. 1991; Renzini et al. 1993). However, the previous measurements of ISM with ASCA have show that the metallicity was less than half a solar (Awaki et al. 1994; Loewenstein et al. 1994; Mushotzky et al. 1994; Matsushita et al. 1994; Arimoto et al. 1997; Matsumoto et al. 1997). Giant early-type galaxies are estimated to have stellar iron abundance of about 1 solar, when observed strong radial gradient of Mg_2 index is taken into account (Arimoto et al. 1997). Thus, the X-ray measured abundances of ISM implied that they were even lower than the stellar metallicity.

The very low metal abundances in ICM cast some doubts in the current scenario of supernova enrichment and chemical evolution of galaxies. Arimoto et al. (1997) discussed various astrophysical aspects of the inferred low iron abundances in the ISM, concerning the chemical evolution of galaxies and cluster of galaxies, the evolution of gas flows in ellipticals, and the heating of the intra-cluster medium. In the attempt of interpreting the observed results in a consistent way, they explored possibilities of hiding or diluting iron in the ISM. However, none of the mechanisms appeared astrophysically plausible, and they alternatively questioned the reliability of using iron-L lines as a diagnostic tool to infer abundances from X-ray spectra. Recently, Buote et al. (1998), Buote et al. (1999) and Buote (1999) reported that some X-ray luminous galaxies have about 1 solar abundance, employing a multi-temperature plasma model.

The high quality X-ray spectra of NGC 4636 (Matsushita et al. 1997) enabled us to study systematic error in our abundance determination, such as the Fe-L atomic physics and abundance ratios. Based on this study, we conclude that the ISM abundance of NGC 4636 is in fact ~ 1 solar. This value is significantly higher than the previous ASCA

results.

Einstein observations have shown that the X-ray luminosities of early-type galaxies scattered by nearly two orders of magnitude, even for the objects with very similar optical properties (e.g. Canizares et al. 1987; Fabbiano et al. 1992). A clue to this long-standing problem has been obtained recently in the deep ASCA observation of the X-ray luminous galaxy NGC 4636, in which a largely extended X-ray emission around the galaxy has been detected. This indicates that NGC 4636 is sitting in the bottom of a large and deep potential structure ($M \sim 10^{13} M_{\odot}$) filled with hot tenuous plasma (Matsushita et al. 1998). This is the main reason why the system has acquired its high X-ray luminousity. ASCA and ROSAT observations of other X-ray luminous galaxies also indicate greatly extended halos (Matsushita 1997; Matsushita 2000). Therefore, the presence or absence of such an extended X-ray halo is considered as the main origin of the large scatter in the X-ray luminosity. Later, Davis and White (1996) discovered a correlation between the metal abundance and temperature in ISM. Loewenstein et al. (1994) report that some X-ray fainter galaxies show significantly lower metal abundances. These features suggest that the problem of low metal abundance may be related with the scatter of X-ray luminosity.

In this paper, we re-examine ISM metallicity in many early-type galaxies including NGC 4636 and discuss the origin of metals based on the relation between ISM metallicity and ISM luminosity. In section 2, we summarize ASCA observations of relevant galaxies. Section 3 deals with conventional data analysis and results, and in section 4, we examine systematic uncertainties in the abundance measurements such as abundance ratios and Fe-L atomic physics. In section 5, we improve the spectral analysis based on the result of section 4 and study correlation between the ISM metallicity and the ISM luminosity. Section 6 gives discussion of the obtained results.

In this paper we adopt for the solar iron abundance the 'meteoritic' value, Fe/H $= 3.24 \times 10^{-5}$ by number (Anders and Grevesse 1989).

2.   Targets and Observations

In the ASCA archival data, we selected early-type galaxies with distances less than 70 Mpc ($H_0 = 75$ km s^{-1} Mpc^{-1}) and B-band luminosities $L_{\rm B} > 10^{10} L_{\odot}$. Objects hosting X-ray bright Active Galactic Nuclei (AGN) and M87, the cD galaxy of the Virgo Cluster, are excluded. The sample constructed in this way consists of 27 galaxies: 6 S0's and 21 ellipticals, as listed in table 1. Our sample is not complete but contains most of the near-by bright galaxies. Ten galaxies are located in cluster environments (Virgo and Fornax clusters) while the others are in the

field. The sample contains one cD galaxy, NGC 1399 in the Fornax cluster. Distances to the galaxies are taken from

Tully (1988) if they are listed, or otherwise calculated assuming the Hubble constant of $H_0 = 75$ km s^{-1} Mpc^{-1};

which generally gives values consistent with the Tully's data.

Table 2 summarizes observational log of the sample galaxies. Most of them were observed for ~ 40 ks. The longest

observation was made for NGC 4636 (Matsushita et al. 1997): ~ 40 ks in PV phase (1993), and ~ 200 ks in AO4

(1995-1996). All the observations were carried out with the SIS and the GIS (Ohashi et al. 1996; Makishima et al.

1996) together. The SIS observing mode is summarized in table 2.

3.   Conventional Spectral Analysis

3.1.   Spectral data

The data are all screened with the standard criteria; namely, data with cosmic-ray cutoff rigidities less than 6

GeV c^{-1} or with elevation angles less than 5° were excluded. We also discarded the SIS data when the elevation

angle from the sun-lit earth was less than 30°. The response matrices consist of RMF and ARF files. We employ

gisv4_0.rmf for the GIS RMF file. Since the SIS response varies with time, the SIS RMF for each observation has

to be individually prepared using SISRMGv1.0. The ARF files have been produced for each observation for the SIS

and GIS, assuming that each target galaxy is a point source. The spectral analysis uses the XSPEC_v9.0 package.

We accumulated on-source spectrum for each galaxy within 4 times r_e, where r_e is the effective radius (from the

RC3 Catalog) centered on each galaxy. When $4r_e$ is less than 3′, the accumulation radius is set to 3′ which covers

80% of the incident X-ray photons from a point source. The background spectrum (Cosmic X-ray Background

and Non X-ray Background) was calculated for each galaxy by integrating the blank-sky data in the same detector

region. A 5% systemic error in the CXB brightness fluctuation (Ishisaki 1996) is included in the background error

in a quadratic form.

The galaxies in the Virgo and the Fornax clusters are surrounded by strong cluster emission, which needs to be

subtracted to obtain the pure galaxy component. Similarly, the data for NGC 499 are affected by the extended

emission in the NGC 507 group. Therefore, for NGC 499, NGC 1404, NGC 4374, NGC 4365, NGC 4406 and

NGC 4552, we derived background spectra from the source pointing data. The background spectra in these cases

were accumulated in off-source regions with the same area and a similar distance from the optical axis as the on-

source integration region to match the statistical weight with the on-source data. For NGC 1404, the off-source

region is also at the same distance from NGC 1399 to cancel the ICM contribution peaked at NGC 1399.

We jointly fit the SIS and GIS spectra with the standard two component model (see Awaki et al. 1994; Matsushita

et al. 1994), consisting of a thin thermal emission and a thermal bremsstrahlung. The former component describes

the emission from the hot ISM, and the model parameters are temperature kT and metallicity. The latter component,

with its temperature fixed at 10 keV, represents the contribution from low-mass X-ray binaries (Matsushita et al.

1994). The two components are allowed to have free normalization, but are subjected to a common absorption by a

free column density N_H.

3.2. Single-temperature fits with solar abundance ratios

The first step of the analysis is fitting the ISM spectra (or soft component) with the Raymond & Smith (1977;

hereafter R-S model) model assuming solar ratios of metal abundances. For weak sources with the soft component

flux less than 6.0×10^{-13}erg s^{-1} in 0.5-10.0 keV, the hydrogen column density is fixed to the Galactic line-of-sight

value because spectral fits cannot constrain temperature and absorption simultaneously.

Results of the spectral fits are summarized in table 3; Fig. 1 shows the SIS spectra of two representative galaxies with

different X-ray luminosities. As shown in the previous ASCA papers (e.g. Matsushita et al. 1997), the spectra can

be well described by the two-component model. However, the fits are statistically unacceptable for X-ray luminous

galaxies (Table 3). The large χ^2 values mostly come from the discrepancy between the data and the model around

the Fe-L complex (0.7 $\sim$ 1.4 keV), which is clearly seen in the SIS data (Figure 1). We will address this problem

later.

As shown in figure 2, X-ray luminosities of the ISM emission in 0.5–10.0 keV (i.e. the soft component), L_{Xs},

within the accumulated radii ($r < 4r_e$), differ very much from object to object, even if their optical properties are

similar. In contrast, the hard-component luminosities, L_{Xh}, show rather good correlation with L_B (figure 2). This

supports our basic interpretation (Matsushita et al. 1994) that the hard component is emitted from binary X-ray

sources in the host galaxy, particularly low-mass X-ray binaries (LMXBs), since the number of binary X-ray sources

(mostly involving neutron stars) should be roughly proportional to its total stellar content. We note however that

several galaxies such as NGC 507, NGC 5084, IC 4296 and IC 1459 exhibit at least a factor of 2 higher L_{Xh}/L_B

ratios than other galaxies. These excess hard X-rays are likely to come from their low-luminosity active nuclei (e.g.

Sadler et al. 1989), and if we exclude these galaxies, L_{Xh} correlates even better with L_{B}. The average $L_{\mathrm{Xh}}/L_{\mathrm{B}}$ ratio is $10^{-3.81}$, excluding objects with $L_{\mathrm{Xh}}/L_{\mathrm{B}} > 10^{-3.34}$. This value agrees very well with the X-ray luminosities of early-type spirals ($L_{\mathrm{X}} = 10^{-3.82}L_{\mathrm{B}}$) obtained with *Einstein* (Fabbiano et al. 1988; Canizares et al. 1987), in which X-ray emission is considered to be dominated by the LMXB emission. Therefore, the large scatter in the X-ray luminosities of early-type galaxies discovered by *Einstein* is mainly attributed to the scatter in L_{Xs}.

Temperatures of the soft component (kT_s) turn out to be 0.3–1.2 keV, and roughly correlate with stellar velocity dispersions, σ (Figure 3). This feature implies that the ISM is primarily heated and confined by the gravity, and, therefore, kT_s reflects the depth of the gravitational potential of each galaxy.

Figure 4 shows relation of L_{Xs} (in $r < 4r_e$) to the soft component temperature kT_s. A clear positive correlation with a correlation coefficient of 0.6, is seen. Since kT_s is a good indicator of the potential depth, this correlation shows that the ISM luminosity within the optical radii is also an indicator of the gravitational potential configuration. This temperature-luminosity correlation for early-type galaxies is much steeper than, and distinct from, that of cluster of galaxies which is plotted in the same figure. This suggests that there is some fundamental difference in the mechanism of hot-gas confinement between galaxies and clusters.

The hydrogen column density N_{H} derived from the spectral fit is mostly consistent with the Galactic values. Exceptions are NGC 1399, NGC 4472, and NGC 7619, in which the measured column densities are about $(1-2) \times 10^{21}\mathrm{cm}^{-2}$.

The single-temperature R-S model assuming solar abundance ratios gives low metal abundances for the ISM, which are 0.1–0.8 solar. A strong positive correlation is seen between the ISM abundance and the ISM temperature, or between the abundance and the ISM luminosity, as shown in figure 5. These correlations are also noticed in the ROSAT data (Davis et al. 1996 Fig.2). The average stellar iron abundance in giant elliptical galaxies is about 1.0 solar (Arimoto et al. 1997). Therefore, in the most X-ray luminous galaxies, the ISM abundance is almost consistent with the stellar metallicity. However, X-ray fainter galaxies indicate the lower ISM abundance than the stellar metallicity, which is very difficult to interpret. Also, there seems no contribution from metal-rich ejecta of type Ia SNe (e.g. Loewenstein et al. 1991; Ciotti et al. 1991; Renzini et al. 1993) in the ISM of all the observed galaxies.

To find some clues for this metallicity problem, we looked at ASCA data of NGC 5018 which indicated extremely low $\mathrm{Mg_2}$ indices. However, this galaxy turned out to be very faint in X-rays (see table 2), consistent with the correlation between L_X/L_B and Mg2 index (Eskridge et al. 1995). Thus, the data could not constrain its ISM

abundance.

The luminosity and abundance values obtained here agree with the published ASCA results (Awaki et al. 1994; Matsushita et al. 1994; Mushotzky et al. 1994; Loewenstein et al. 1994; Matsumoto et al. 1997; Arimoto et al. 1997; Buote et al. 1998; Buote et al. 1999; Buote 1999). This paper uses the 'meteoritic' value for the definition of the solar Fe abundance: the number ratio of Fe/H to be 3.24×10^{-5}. The previous papers all use the 'photospheric' value, 4.68×10^{-5}. The 'meteoritic' value is directly obtained from meteorites, while the 'photospheric' one involves spectral analysis of solar photosphere (Anders & Grevesse, 1989). Thus, the former is considered more reliable than the latter.

We should emphasize that the ASCA data are the first to enables us to separate the soft and the hard spectral components unambiguously. The previous missions did not have necessary spectral resolution or hard X-ray sensitivity. The ASCA results obtained here are generally consistent with the previous results by it Ginga (Awaki et al. 1991; Ikebe et al. 1992), BBXRT (Serlemitsos et al. 1993), and $ROSAT$ (Trinchieri et al. 1994; Forman et al. 1993; Davis and White 1996; Fabbiano et al. 1994).

As a brief summary, we confirmed that the X-ray spectra of early-type galaxies show very low metal abundances. X-ray luminous galaxies indicate large χ^2 values in the spectral fits, which is also a problem. In the following subsections, we attempt to address these problems based on conventional spectral analysis.

3.3. Multi-temperature model

The spectral fits with single temperature models were performed in section 3.2. However, $ROSAT$ observations of X-ray luminous galaxies show that the projected temperature profiles have significant gradients by ~ 0.2 keV (e.g. Trinchieri et al. 1994; Matsushita 2000), although gradients for X-ray fainter galaxies are smaller (Matsushita 2000). Even when there is no large-scale inhomogeneity, the ISM may have a temperature fluctuation in small angular scales. The central regions of clusters of galaxies in fact often show multi-temperature components, such as that in the Centaurus cluster (Fukazawa et al. 1994; Ikebe et al. 1999).

Buote and Fabian (1998), Buote et al. (1999), and Buote (1999) report that spectral fits with two-temperature or multi-temperature model for early-type galaxies commonly give larger metal abundances than the single-temperature fits. We tried similar models on the SIS and GIS spectra, assuming multiple R-S components and the 10 keV bremsstrahlung. Before fitting the actual data, we carried out simulations. Multi-temperature spectra with similar

statistical quality as the data were constructed and fitted with various models. Single-temperature models were found to give approximately an average temperature and metal abundance when the temperature range of the multi component was within ~ 0.2 keV. Based on this result, the fitting models were made up as a sum of seven R-S components with fixed temperatures of 0.2, 0.4, 0.6, 0.8, 1.0, 1.2 and 1.4 keV, and a 10 keV bremsstrahlung for the hard component. The seven R-S components were constrained to have a common abundance, but were allowed to have separate, free normalizations. The overall model was subjected to absorption with a common photoelectric absorber. The column density was left free for X-ray brighter galaxies and fixed to the Galactic value for fainter ones, in the same way as in the previous subsection. Further addition of different temperature components did not change the result. Thus, these 7 temperatures are practically enough to reproduce the metal abundance for any given multi-temperature model, and this model is more universal than the two or three temperature model in describing the multi-temperature nature of the ISM.

The fitting results are summarized in Table 3 and shown in figure 6 and 7, compared with the previous single temperature fits. The 2 models give very similar χ^2 values (figure 6). This simply indicates that the large χ^2 values for X-ray luminous galaxies are not caused by an incorrect modeling of multi-temperature emission. As reported by Buote et al. (1998), the 7-temperature fit increases metal abundance for NGC 1399 and NGC 4472 by 50%. However, the increment is only 10–20% in other X-ray luminous galaxies, and the average metal abundance for all the luminous galaxies increases only by $\sim 30\%$ (figure 7). The uncertainty is larger for X-ray fainter galaxies because of the increased degree of freedom in the temperature space. However, temperature gradients are smaller in the fainter galaxies as shown in Matsushita (2000).

We conclude that the low abundance problem in the previous section cannot be solved by the multi-temperature model, at least in the several X-ray luminous galaxies.

3.4. Deviation from ionization equilibrium

The major assumption we have adopted is that the ISM is in a complete ionization equilibrium. Generally, the degree of ionization of a plasma is parameterized by the quantity nt (Masai 1984), which is a product of the electron density n and the elapsed time t measured from the initial time of ionization when the gas was neutral. The plasma reaches an ionization equilibrium when nt exceeds $\sim 10^{12}$ cm^{-3} s. Since the electron density in the ISM of early-type galaxies is typically $n = 10^{-1} \sim 10^{-3}$ cm^{-3} (Forman et al. 1985; Trinchieri et al. 1986; Canizares et al. 1987), the

ionization equilibrium is attained in only $3 \times 10^{5 \sim 7}$ yr. The ISM should, therefore, be in a complete ionization equilibrium. However, there is a possibility that the metals are locked in dust grains, which may be able to explain the observed low metallicity in the ISM. These dust grains are sputtered by hot electrons in the ISM and gradually ionized. The time scale for the grain evaporation is similar to the above ionization equilibrium time scale (Itoh 1989; Masai 1984), so the spectral features should indicate deviation from ionization equilibrium if dust sputterings are still going on.

Among the plasma emission codes, only Masai model deals with plasmas in non-ionization-equilibrium (NIE) condition. With this NIE model, we fitted the SIS and GIS spectra of all the sample galaxies, similarly as in section 3.2. The derived temperature and abundance will be separately examined later in section 4.2. Figure 8 summarizes the derived nt parameter as a function of best-fit temperatures. Most of the objects consistent to have $nt \sim 10^{12}$ cm^{-3} s, implying that the ISM is in an ionization equilibrium.

4.   Problems in the Spectral Analysis

As shown in section 3, no solution was given to the low-abundance problem by the multi-temperature models or by the consideration of non-ionization equilibrium. The remaining points we need to examine are deviation of abundance ratios from the solar values and uncertainty in the Fe-L atomic physics.

4.1.   Uncertainty in the abundance ratios

Abundance ratios provide key information about the origin of the ISM. However, deriving elemental contributions from an X-ray spectrum is a complicated task for a temperature $kT \sim 1$ keV. Figure 9 shows the best-fit R-S model for the NGC 4636 data decomposed into the constituent elements. A major part of the emission comes from Fe-L complex. Considerable contribution comes from K-emission lines of lighter elements, such as O, Ne, Mg, Si, and S. Furthermore, Ni-L lines overlap with the Fe-L complex. Another problem is caused by free-bound emission, which gives a step-like addition on the bremsstrahlung continuum at the energies of K and L-edges of each element. These spectral features due to free-bound continuum and emission lines in a single spectrum have to be fitted in a consistent manner in obtaining the metal abundance.

To avoid the complexity in the spectral fit as much as possible, we have combined the elements heavier than H and He into two groups. One group consists of α-elements, O, Ne, Mg, Si and S. A single common abundance is

assigned to these elements, which is hereafter denoted by A_α. The other group consists of Fe and Ni, and their common abundance is denoted by $A_{\rm Fe}$. This grouping was successfully applied to the data of NGC 4636 (Matsushita et al. 1997). Obviously, the division of elements reflects metal synthesis processes; the former group elements are produced in SNe II and the latter ones in SNe Ia, respectively. Although Si and S are partly synthesized in SNe Ia, at least the ASCA data of NGC 4636 indicate that Mg to Si abundance ratio agrees well with the solar ratio (Matsushita et al. 1997). Therefore, it seems reasonable in the present analysis to assume that all the α-elements (O, Ne, Mg, Si and S) have the same abundance.

The GIS and SIS spectra are jointly fitted with the same model as before, with A_α and $A_{\rm Fe}$ as free parameters. All the galaxies are analyzed in the same way, and the results are summarized in table 4. The χ^2 values show no improvement in this fit (figure 10). Figure 11 shows confidence contours of A_α against $A_{\rm Fe}$ for 8 representative galaxies, in an increasing order of the ISM luminosity. The contours all show narrow elongated shapes, indicating that the two parameters couple strongly. This is mainly because K-lines and free-bound emission from α-elements push up the continuum level for the Fe-L lines. As a result, the uncertainty has increased by several times compared with the case of the solar ratio fit.

For X-ray luminous galaxies the error regions shown in figure 11 are very much underestimated, because their spectral fits are formally unacceptable with reduced χ^2 larger than 1.5. To examine whether much higher abundance is allowed by the data, we forced A_α to 1.0 solar and left $A_{\rm Fe}$ free to vary. The results are summarized in table 4. Figure 12 compares the two fits, In both cases, the data-to-model ratio deviates to a similar extent. The increment of the reduced χ^2 from the previous variable abundance fit is only $\sim 10\%$ even for X-ray luminous galaxies (figure 10). However, the previous fits were not acceptable, either. The additional deviation of the model mainly occurs in the O-K line region. This O-K line problem is in fact much smaller than the deviations already present in the variable abundance fit around 0.7–0.8 keV, namely in the region of Fe-L complex. Therefore, the spectral fit cannot clearly reject the case of $A_\alpha = 1.0$ solar even for X-ray luminous galaxies.

When A_α is fixed at 1.0 solar, $A_{\rm Fe}$ correlates well with the ISM luminosity as shown in figure 13. In this case, $A_{\rm Fe}$ becomes about 1.0 solar in X-ray luminous ($L_X > 10^{41}$ erg s^{-1}) galaxies, and 0.5 solar in X-ray fainter ones. Thus the scatter in the iron abundance among the bright and faint galaxies is now only within a factor of 2, while it was an order-of-magnitude difference in the solar-abundance-ratio fit (see figure 5). We note that there is no difference between S0 and elliptical galaxies. This point will be discussed in section 6.2.3.

To summarize the fitting results, the strong coupling between A_α and A_{Fe} has made the abundance estimation difficult; on one hand, this coupling hampers unique determination of the overall metallicity. On the other hand, if we shift the A_α/A_{Fe} ratio slightly off from the unity, the allowed metallicity becomes significantly higher than the results of solar ratio analysis.

4.2.   Problems in the iron-L atomic physics

The spectral fit is made complicated due to the uncertainty in the Fe-L atomic physics. The abundances reported in the previous subsections have been obtained with the R-S thin thermal plasma emission code. However, the model cannot fit the Fe-L structure of X-ray luminous galaxies, even when we assume the multi-temperature model or allow the abundance ratio to vary. The similar results were reported for the cluster emission by Fabian et al. (1994). As Arimoto et al. (1997) and Matsushita et al. (1997) have investigated, other plasma codes, MEKA (Mewe et al. 1985; Mewe et al. 1986; Kaastra 1992), MEKAL (Liedahl et al. 1995) and Masai (Masai 1984) model, differ from the R-S model mainly in the treatment of the Fe-L atomic physics. When the plasma temperature is lower than ~ 2 keV, these codes give considerably different spectral features (Masai 1997). We need to examine the goodness of the fit and the inferred abundance for these different spectral codes.

By changing the spectral models, we fitted the SIS and GIS data of all galaxies exactly in the same way as described in section 4.1. The double-component model (thermal and hard bremsstrahlung) was assumed with A_α and A_{Fe} as free parameters. We assumed an ionization equilibrium in the fit.

As summarized in Table 5, the results depend heavily on the adopted plasma emission code. As shown in figure 14, the reduced χ^2 values are fairly model dependent for bright galaxies. Figure 12 shows data-to-model ratio for the R-S and MEKAL models in the case of SIS spectra for two X-ray luminous galaxies, NGC 4636 and NGC 4472. Either of the models cannot reproduce the Fe-L complex adequately, and the model-to-data relation is significantly different between the two plasma emission codes.

The physical parameters derived from the spectral fits are also strongly model dependent. Figure 15a compares the ISM temperature and hydrogen column density for different plasma codes. The difference in the temperature is relatively systematic: the MEKA model gives the lowest temperature among the four codes, about 20% lower than the case of R-S model, while MEKAL and Masai models predict temperatures within 10% of the R-S values. As discussed in Masai (1997), the different ionization and recombination rates of Fe mainly causes these discrepancies

in the spectral parameters. The hydrogen column density also depends on the plasma emission codes (figure 15b). MEKA and MEKAL models give consistent or slightly higher values than the R-S model, while Masai model tends to indicate lower absorption. For galaxies with large column densities, the difference sometimes amounts to 10^{21} cm^{-2}.

The metal abundance shows a strong model dependence (figure 16a), with large uncertainty in X-ray fainter galaxies. The MEKAL and the R-S models give similar values of A_α and A_{Fe}, and the MEKA and Masai models indicate systematically higher abundances by a factor of $2 \sim 3$ on the average. In particular, the Masai model gives an abundance up to ~ 2 solar for the most X-ray luminous galaxies.

However, figure 17 shows that the correlation between the two abundance groups, A_α and A_{Fe}, forms a very similar elongated shape for all models as already seen in the case of R-S fit (in section 4.1). In X-ray fainter galaxies, the 4 error regions overlap and the implied abundances are consistent with each other among the plasma codes. In X-ray luminous galaxies, the error regions are aligned in a narrow band which runs almost in parallel to the elongation direction of each region.

As a result, once A_α is given, the difference in A_{Fe} among the models must be fairly small. To confirm this point in a quantitative manner, we fitted the spectra with A_α fixed at 1.0 solar and looked at the difference in A_{Fe}. The results are listed in Table 5 and shown in figure 16b. Clearly, A_{Fe} for different models fluctuates by only 20–30%.

The strong coupling between Fe-L lines and the spectral features due to other light elements is the main factor which complicates the abundance determination. The level of coupling is significantly different among the plasma emission models, which reflects the uncertainty in the Fe-L atomic physics. When A_α is fixed, the difference with the plasma code reduces to only 20–30% as shown in Figure 16b. This means that if we are able to determine the level of the free-bound continuum, the abundance using the Fe-L lines will be effectively constrained.

5. Improved Spectral Analysis

5.1. Spectral fits above 1.6 keV

Based on the study in section 4, we first try to determine A_α which is the common abundance of so-called α-burning elements. Among them, lines from O and Ne are difficult to constrain from the ASCA data due to false coupling between the Fe-L lines and the O-K and Ne-K lines (see section 4.1, section 4.2). In contrast, Si-K and S-K lines are clearly seen in the spectra of X-ray luminous galaxies,

To utilize K-lines of Si and S, we exclude the Fe-L region, which is < 1.6 keV for the SIS and < 1.7 keV for the GIS data, respectively. Because of the effect of free-bound continuum from O, Ne, and Mg, the determination of A_α is not straightforward. We need to assume relative abundance ratios among the α-burning elements. The ASCA data for NGC 4636 indicate that the abundance ratio between Mg and Si agrees with the solar value within $\sim 30\%$ (Matsushita et al. 1997). We assume here the same condition for other X-ray luminous galaxies, namely O, Ne, and Mg are all assumed to have the same abundance. Thus, the fitting model consists again of the 10 keV bremsstrahlung and the R-S model, with the latter employing the same elemental groups of A_α and A_{Fe} (see section 4.1).

The fits turned out to be acceptable (table 6), mainly because the Fe-L region was excluded. The temperature shows a typical error of ~ 0.1 keV, and are broadly consistent with those in the previous fits involving the whole energy range (table 3,4,5). The confidence contours of A_{Fe} vs. A_α for these hard band fits are shown in figure 18 as shaded regions. The omission of the Fe-L region naturally leads to a much larger error of A_{Fe} (figure 18). Nevertheless, A_α has been relatively well constrained with no strong dependence on A_{Fe}. This is because free-bound continuum of Fe-L is weaker than those of O and Ne. In NGC 4636 and NGC 4472, A_α is approximately one solar when A_{Fe} is around one solar. If one tries to raise A_α up to 2 solar, then A_{Fe} would have to be as high as 5 solar as implied by the shaded region in figure 18. In NGC 507 and NGC 1399, A_α is smaller than the level of NGC 4636 for the same value of A_{Fe}. Other X-ray luminous galaxies also show a similar correlation with larger uncertainties.

5.2.   *Additional systematic errors to the Fe-L region*

The successful determination of A_α in section 5.1 has left A_{Fe} poorly constrained, because of the complete ignorance of the Fe-L data which must be very informative. We need somehow to utilize the information carried by the low-energy spectra. The method we take here is recovering the low-energy (< 1.6 keV) data with reduced statistical weight assigned on them. The low statistical weight should prevent the spectral fit from imposing a strong false constraint on A_α, which was formerly resulted when the Fe-L band spectrum was fitted too faithfully. Furthermore, the increased error helps to make the fit formally acceptable and enables us to evaluate the parameter errors in a straightforward manner.

The best-fit models show difference from the data in the Fe-L region with a typical amplitude of $\sim 20\%$ for X-ray luminous galaxies (figure 12). The deviation patterns are significantly different among the models. When A_α is

fixed, the variation of A_{Fe} with the plasma code also becomes $20 \sim 30\%$. This level of variation is also expected from the theoretical consideration by Masai (1997). Based on these features, we will introduce an additional systematic error of 20% in the 0.4–1.6 keV region. This level of error still keeps the ability of spectral data to constrain the model in the Fe-L region with reasonable strength, as show below.

With this procedure, all the spectral fits have become acceptable for all emission models (table 7). The additional 20% error was confirmed to be appropriate, since an error level of 10% gives too large χ^2 (reduced $\chi^2 > 1.5$) and 30% gives too low χ^2 (reduced $\chi^2 < 0.7$) values, respectively. The derived temperature and hydrogen column density are consistent with the previous results. The confidence contours for A_α vs. A_{Fe}, shown in Figure 18, are still elongated, but different plasma emission codes now indicate overlaps with each other. This feature enables us to estimate confidence regions for A_α and A_{Fe}. NGC 4636 indicates both abundances to be ~ 1 solar within a factor of 2. Other X-ray luminous galaxies show A_α and A_{Fe} to be $0.5 \sim 1.0$ solar. The ratio of A_α to A_{Fe} is within $\pm 50\%$ of the solar value at the 90% confidence for all galaxies. These abundance values differ significantly from those obtained with the exact solar-ratio assumption described in section 3.2. The A_α values agree well with the hard-band results in the previous subsection. This consistency supports that our treatment of the data in the Fe-L region is appropriate.

5.3. Correlation between ISM metallicity and luminosity

Correlation between the metallicity and the X-ray luminosity of the ISM needs to be examined again. X-ray fainter galaxies show very weak lines from α elements (see figure 1), and their soft X-ray continua are masked by rather strong hard components. These conditions hamper accurate determination of A_α in these galaxies, also making A_{Fe} values highly uncertain.

In order to cope with this difficulty in the X-ray fainter galaxies, we have combined the data of all target galaxies into 6 groups according to their ISM temperature and X-ray luminosity as shown in Table 8. The spectra in each group are fitted simultaneously. The ISM temperature and 2 normalization parameters for the soft and hard components are free parameters assigned for each galaxy, while all the galaxies are assumed to have common A_α and A_{Fe} values. The 20% systematic error is included in the Fe-L region for X-ray luminous galaxies ($L_X > 10^{40}$ erg s^{-1}), but X-ray fainter galaxies ($L_X < 10^{40}$ egs s^{-1}) go through the fitting directly because statistical errors are much larger.

The results from this group analysis are summarized in table 8 and shown in figure 19. Acceptable fits are obtained

for all groups with the parameter values consistent with those derived in section 5.2. X-ray luminous galaxies give consistent results for all the plasma emission codes. The confidence contours for X-ray fainter galaxies indicate large uncertainties for both A_α and $A_{\rm Fe}$, similar to the features in figure 11. For a given A_α, however, the power of constraining $A_{\rm Fe}$ has become better.

All the plasma emission codes show separation of confidence contours for the faint and the luminous groups. X-ray luminous galaxies indicate $A_{\rm Fe}$ and A_α to be $0.5 \sim 1$ solar, and their ratio is within $\sim 30\%$ of the solar value. The X-ray fainter galaxies show significantly lower $A_{\rm Fe}$ for the same A_α. When the ISM temperatures are similar, the strength of Fe-L lines directly indicates the abundance difference. The abundance comparison between X-ray luminous and faint low-temperature ($0.6 < kT < 0.8$ keV) groups should, therefore, involve very small systematic error. We conclude that the ISM abundance depends more on the ISM luminosity than on the ISM temperature.

Among X-ray luminous galaxies, the high temperature group indicates low A_α and $A_{\rm Fe}$ values at ~ 0.5 solar. Representative galaxies are NGC 507 and NGC 1399, which show low A_α values determined from Si K-line intensity for a given value of $A_{\rm Fe}$ as shown in figure 18. The abundance ratio is similar to those in the other X-ray luminous groups.

6.   Discussion

We have analyzed ASCA data for 27 giant ($L_B > 10^{10} L_\odot$) early-type galaxies. X-ray luminosities of these galaxies are $10^{40 \sim 42}$ ergs^{-1}.

6.1.   Summary of results

The spectra of the early-type galaxies have been fitted reasonably well with a $0.3 - 1.0$ keV thermal model (the soft component) and a 10 keV bremsstrahlung model (the hard component). The hard component should mostly consist of emission from LMXBs such as in early-type spirals and in galactic bulges. By separating the pure ISM component, we showed that the large scatter in the overall X-ray luminosity of these objects was due to fluctuations in the ISM luminosity.

Unusually low abundances (~ 0.3 solar) were obtained with the R-S plasma model assuming solar-abundance ratios. We carefully examined whether these results are artifacts of the data analysis. We showed that multi-temperature models could not change the results of the most X-ray luminous galaxies, alghouth higher abundances

were allowed for X-ray fainter galaxies simply because of poor data statistics. Assumption of non-ionization equilibrium could not solve the problem either.

We found that the overlap among emission lines and free-bound continuum cause strong coupling among the abundances of various elements. As a result, when models with variable abundance ratios are fitted to the data, the allowed range of abundance increases dramatically while keeping strong correlations among different elements. Another difficulty is the large uncertainty in the Fe-L atomic physics. Different plasma emission codes give significantly different abundances, and none of them provide acceptable fits to the Fe-L spectra of X-ray luminous galaxies. In contrast, when abundances of α-elements (A_α) were fixed, all the plasma codes give similar Fe-abundances (A_{Fe}) within 20–30%. Therefore, the strong dependence of the abundance on the emission code is mainly attributed to the strong coupling between Fe-L and α-element lines (particularly O-K and Ne-K lines).

In order to solve the above coupling problem, we have assumed α-elements to take the solar abundance ratios based on the results by Matsushita et al. (1997). Effect of the free-bound emission of Fe-L on the Si abundance was estimated, and the Si abundance was concluded to be roughly 1 solar within a factor of 2 in X-ray luminous galaxies. Finally, we included additional systematic errors by 20% in the Fe-L region of the spectra and relaxed the strong coupling between Fe and α-elements (particularly O and Ne). This has allowed the Si-K lines to make a significant contribution to the χ^2 minimization for several X-ray luminous galaxies, and as a consequence, the derived A_α and $A_{\rm Fe}$ both became ~ 1 solar within a factor of 2. In addition, discrepancy among the plasma emission codes has been reduced, and the spectral fits have become mostly acceptable with all plasma models.

In contrast to the luminous objects, the ISM metallicity in X-ray faint galaxies remained highly uncertain because of very large statistical errors in the Si line intensity. However, strong correlation was again seen between Fe and α-element abundances, and the $A_{\rm Fe}$ vs. A_α confidence regions showed statistically significant dependences on the X-ray luminosity.

6.2. ISM metallicity and chemical evolution

The hot ISM is considered to be a mixture of the stellar mass-loss products and the supernova ejecta. Therefore, elemental abundances in the ISM measured with X-ray spectra give almost unique information on the contribution from these enrichment processes.

More specifically, the ISM abundances can be expressed as,

$$z^i = \frac{\alpha_* y_*^i + \alpha_{\rm SN} y_{\rm SN}^i}{\alpha_* + \alpha_{\rm SN}} \sim y_*^i + \langle \frac{\alpha_{\rm SN}}{\alpha_*} \rangle y_{\rm SN}^i \tag{1}$$

(Loewenstein and Mathews 1991; Ciotti et al. 1991), where z^i is the mass fraction of the ith element, α_* and $\alpha_{\rm SN}$ are the mass loss rates of stars and SNe respectively, and y_*^i and $y_{\rm SN}^i$ are their yields.

6.2.1.   Is the ISM Diluted by the ICM?

We first check the validity of equation (1) in which we assume that the whole ISM in a galaxy consists of matter supplied by the stellar component of the galaxy itself. Elliptical galaxies are often surrounded by a hot ICM, which can be accreted if an inflow is established, and dilute the indigenous ISM (Renzini et al. 1993).

Eskridge et al. (1995) discovered a strong correlation between L_X/L_B and potential depth, or stellar velocity dispersion. Later, the existence of largely extended X-ray emission around some X-ray luminous galaxies such as NGC 4636 (Matsushita et al. 1998) and NGC 1399 (Ikebe et al. 1996) suggests that these galaxies are located in the bottom of a largely extended potential well filled with a tenuous plasma. If surrounding metal poor gas is accreting onto a galaxy, the galaxy becomes overluminous in X-rays, as the additional PdV work by the infalling material needs to be radiated away in a quasi-stationary cooling flow and become metal poor. Actually, the most luminous objects, NGC 507, which is surrounded by diffuse extended group ICM (Trinchieri et al. 1997), and NGC 1399 tends to have slightly lower ISM abundance than the other X-ray luminous galaxies. The similarity of A_α to $A_{\rm Fe}$ ratio among the X-ray luminous objects suggests that the low metallicity in the most luminous objects may be slightly more diluted by metal poor gas than other X-ray luminous galaxies.

X-ray fainter objects show small scatter of $A_{\rm Fe}$ for a given level of A_α, as shown in figure 13. The sample contains objects surrounded by dense ICM, such as NGC 1404 and NGC 4374, and also relatively isolated galaxies, such as NGC 720 and IC 1459. This suggest that the ISM in the X-ray faint objects are not significantly diluted by ICM. As summarized in figure 19, X-ray luminous objects show higher metal abundance than X-ray fainter ones. Therefore, dilution may well occur in the X-ray luminous objects, and in this case the abundance difference between the luminous and faint galaxies becomes even larger.

6.2.2.   Constraints on the SNe Ia rate

From the equation (1), combining the latest observed SNe Ia rate with the Hubble constant of 75 kms^{-1}Mpc^{-1} (Cappellaro et al. 1993; Cappellaro et al. 1997; Tammann et al. 1995; van den Bergh et al. 1991), with a nucleosynthesis calculation by Thielemann et al. (1996) and a stellar mass loss rate by Ciotti et al. (1991), the abundance of Fe enriched only by the SNe Ia is predicted to be 2 solar.

The measured Fe abundance actually consists of contributions from SNe II and SNe Ia; the former one is supplied via stellar mass loss, while the latter are by SN mass ejection and by stellar mass loss, since we do not know whether stars contain SNe Ia products or not. If we would explain the observed Fe abundance in terms of SNe Ia only, then it gives an upper limit of the SNe Ia rate. The SNe II ejecta are estimated to have an abundance ratio $A_\alpha/A_{\rm Fe} \sim 3$ (e.g. Thielemann et al. 1996), while SNe Ia products have $A_\alpha \ll A_{\rm Fe}$. Si and S can be supplied by both SNe II and SNe Ia, but the latter contribution should be negligible as long as the SN Ia rate is low. Thus, contribution from SNe Ia to $A_{\rm Fe}$ ($A_{\rm FeSNIa}$) is estimated as

$$A_{\rm FeSNIa} = A_{\rm Fe} - 1/3A_\alpha. \tag{2}$$

On the A_α vs. $A_{\rm Fe}$ plane, we draw lines of $A_{\rm Fe} = {\rm const.} + 1/3{\rm A}_\alpha$ as shown in figure 19 by dotted lines. Each line indicates a constant contribution from SNe Ia.

The large uncertainty in A_α in figure 19 indicates that the contribution of SN II is highly ambiguous. However, the confidence contours for A_α vs. $A_{\rm Fe}$ are rather narrow along the lines of constant SN Ia contribution. This is most clearly seen for X-ray fainter galaxies. This means that the contribution of SN Ia is well constrained by the data. By extrapolating these contours along the dotted lines in figure 19 to a small A_α value, we can estimate the SN Ia contribution to $A_{\rm Fe}$. X-ray fainter galaxies indicate the iron abundance attributable to SN Ia, $A_{\rm FeSNIa}$ inferred from equation (1), to be less than 0.2 solar for R-S, MEKA, and MEKAL models, and $0.2 \sim 0.5$ solar for Masai model, respectively. In contrast, X-ray luminous galaxies show $A_{\rm FeSNIa}$ to be about 0.5 solar for RS, MEKA, and MEKAL and ~ 1 solar for Masai model, respectively. With the slight difference among the plasma emission codes, we can conclude that the SN Ia contribution to $A_{\rm Fe}$ is positively correlated with the X-ray luminosity.

Taking the result by Masai model, which gives the highest Fe abundance, the upper limit of the inferred SNe Ia rate is a factor of 2 and 5 smaller than the Cappellaro's value for the X-ray luminous and fainter galaxies, respectively. As mentioned in section 6.2.1, the ISM in X-ray luminous objects may be simply diluted by ICM. However, the low

Fe abundance in X-ray fainter galaxies is a severe problem which contradicts with the SN rate.

6.2.3.   Constraint on stellar metallicity

Optical measurements of stellar metallicity in giant early-type galaxies have been performed only within $\sim 1r_e$. In our sample galaxies, the average stellar metallicity over an entire galaxy is typically $0.5 \sim 1$ solar taking into account the observed metallicity gradient beyond $\sim 1r_e$ (Arimoto et al. 1997; Kobayashi et al. 1999). Stellar metal ratios are reported to be SNe II-like at least in the center of galaxies (Worthey et al. 1992; Kobayashi et al. 1999).

X-ray observations are able to constrain stellar metallicity over an entire galaxy, which is hardly performed with optical observations. Based on equation (1), $A_{\rm Fe}$ gives an upper limit of the stellar Fe abundance. A_α, on the other hand, directly reflects the stellar α-element abundance, since SNe Ia contribution is negligible even for Si and S. X-ray luminous galaxies show both $A_{\rm Fe}$ and A_α to be ~ 1.0 solar, which is fairly close to the stellar levels. A few galaxies such as NGC 507 indicate somewhat lower ISM abundance. Thus, the previous severe discrepancy, that the ISM metallicity is even lower than the stellar metallicity (e.g. Awaki et al. 1994; Arimoto et al. 1997), has been mostly removed based on our improved analysis.

Since Mg_2 indices and colors are similar for all the observed galaxies (Kodama and Matsushita 2000), it is reasonable to assume that X-ray fainter galaxies have similar stellar metallicity to those in X-ray lumious galaxies. In this case, A_α, which directly reflects the stellar α-element abundance, should be ~ 1.0 solar in these galaxies. If ISM is diluted in X-ray luminous objects, the α-element abundance in the fainter galaxies may be even higher. Now, figure 19 implies a larger SN II contribution to ISM in more luminous systems, which should mainly come from stellar mass loss. This feature leads us to predict that stellar metallicity in giant early-type galaxies should be SNeII-like even when averaged over the whole galaxy.

We can also constrain stellar metallicity in S0 galaxies. There are 5 S0 galaxies in the X-ray fainter group, and we do not detect any difference in the ISM abundance between S0 and elliptical galaxies (figure 13). These S0 galaxies show Mg_2 indices close to those of elliptical galaxies. Therefore, abundances of α-elements in the stars in S0 galaxies should be similar within a few tens of % to those in elliptical galaxies. If stellar iron abundance is different between S0 and elliptical galaxies, it should be reflected as a significant difference in the ISM abundance, contrary to the observed feature. Therefore, stellar metallicity in S0 galaxies is considered to be similar to that in elliptical galaxies. This conclusion gives an important constraint in modeling the origin and evolution of S0 galaxies.

6.2.4. Relation to metals in the ICM

It has been recognized that the hot ICM in clusters of galaxies contains a large amount of iron (Hatsukade 1989; Tsuru 1993; Fukazawa et al. 1998). Clearly, this iron must have been supplied by member galaxies, with early-type galaxies as main contributors (Arnaud et al. 1992).

In evaluating the metal enrichment process independently of the amount primordial gas, it is convenient to introduce "iron mass to light ratio" (IMLR), which is the ratio of the total iron mass in a cluster ICM over the total optical luminosity of cluster galaxies. The observed value of IMLR appears to be remarkably constant among the clusters at $0.01 - 0.02$ (Tsuru 1993; Arnaud et al. 1992; Renzini 1993). This IMLR level is too high to be explained by the stellar mass loss from member galaxies (Tsuru 1993). The total released mass from stars over the Hubble time is $10 \sim 20\%$ of the stellar mass in a galaxy, and its contribution to the cluster IMLR is estimated to be $(1-2) \times 10^{-3}$ assuming the metallicity of the mass-loss gas to be about 1 solar. This is only $\sim 1/10$ of the observed IMLR in the ICM. Therefore, the supernova enrichment is definitely required to explain the observed IMLR.

The IMLR values are calculated for the ISM, based on our updated abundance determination, and compared with the cluster level in figure 20. The ISM mass within $4r_e$ is estimated from a single β model, assuming $\beta = 0.5$ and a core radius $= 1$ kpc which are typical values obtained by *Einstein* (Forman et al. 1985; Trinchieri et al 1986). Individual galaxies indicate low IMLR values compared with clusters. This is not surprising in a sense, because the ISM mass is at most a few percent of the stellar mass while the ICM is 2–5 times more massive than the stellar content in clusters. An important feature seen in figure 20 is that the stellar mass-loss and SNe Ia can release only $\sim 20\%$ of the total stellar mass in the Hubble time (e.g. Renzini et al. 1993). Therefore, with the present ISM metallicity in the outflow, the accumulated IMLR would reach at most 10 times higher level and unable to explain the observed cluster metals. In this view, the ISM metallicity is too low regardless of the estimated supernova rate.

This consideration suggests that the ISM metallicity may not directly reflect the SN Ia rate, even though the measured values themselves are secure quantities.

6.3. Interpretation of the remaining problem, low SNe Ia contribution

The discrepancy between stellar and ISM abundances has been mostly removed. There are various models which try to explain how a large amount of Fe in ICM could have been synthesized even with the present SNe Ia rate, including the Capperaro's value (e.g. Renzini et al. 1993; Arimoto et al. 1997; Ishimaru 1997). Considering the large

Fe contribution from SNe Ia to the ICM (Fukazawa et al. 1998), the SNe Ia rate must have been higher in the past. We need to examine if this picture can explain why SNe Ia contribution is lower in the X-ray fainter galaxies, as shown in figure 19.

Since X-ray luminous and X-ray fainter galaxies show similar optical properties (Kodama and Matsushita 2000), the difference in the metal abundance cannot be simply explained by the present SN Ia frequency.

The larger amount of ISM in X-ray luminous galaxies suggests a longer accumulation time. In this case, the higher metal abundance may reflect a gradual change in the SN Ia rate in the past. However, as shown in figure 20, within the optical radii, the gas mass in X-ray luminous galaxies is only a few % of the stellar mass. This means that it takes only a few Gyr to build up the ISM with the present stellar mass loss rate (e.g. Ciotti et al. 1991) even in the luminous galaxies. A quick decline in the type Ia supernova rate in such a short time scale is very unlikely.

We propose here that the low SN Ia contribution in the ISM of X-ray fainter galaxies is due to a loss of SN Ia products to the intergalactic space (see also Fujita 1997). This is mainly caused by the shallow gravitational potential. The stellar mass-loss component may also escape from these systems in the form of a mild outflow (Ciotti et al. 1994). The SN Ia products would escape together with the mass-loss gas or may have higher escaping probability than it. In X-ray luminous galaxies, the extended gravitational potential (Matsushita 1997; Matsushita et al. 1998) would trap considerable fraction of the supernova product. Therefore, the spatial extent of SN Ia products probably reflect the overall potential structure beyond the optical scale. In closing, we should note that the dynamical motion of supernova bubbles in early-type galaxies may be significantly different from that in spirals. Progenitors follow a random velocity field in early-type systems instead of the disk rotation, and the ambient pressure is dominated by the hot plasma (i.e. ISM) rather than by cold interstellar gas. We hope future high resolution imaging and spectroscopy in X-rays will bring us rich information about the motion and structure of metal-rich gas in early galaxies.

References

Anders E., & Grevesse N., 1989, gca, 53,197

Arimoto, N., Matsushita, K., Ishimaru, Y., Ohashi, T., & Renzini, A. 1997, ApJ, 477, 128

Arnaud, M., et al. 1992, A&A, 254, 49

Awaki, H., Koyama, K., Kunieda, H., Takano, S., Tawara, Y., & Ohashi, T. 1991, ApJ, 366, 88

Awaki, H. et al. 1994, PASJ, 46, L65

Buote, D. A., and Fabian A.C., 1998, MNRAS, 296,977

Buote, D. A., 1999, MNRAS, 309, 685

Boute, D. A., Canizares, C. R., & A. C. Fabian,2000, MNRAS, 310, 483

Canizares, C.R., Fabbiano, G., & Trinchieri, G. 1987, ApJ, 312, 503

Cappellaro, E., Turatto, M., Benetti, S., Tsvetkov, D. Yu., Bartunov, O. S., & Makarova, I. N. 1993, A&A , 273,
    383

Cappellaro, E., Turatto, M.; Tsvetkov, D. Yu.; Bartunov, O. S.; Pollas, C.; Evans, R.; Hamuy, M., 1997, A&A, 322,
    431

Ciotti, L., Pellegrini, S., Renzini, A., & D'Ercole, A. 1991, ApJ, 376, 380

Davis D.S., White R.E., 1996, ApJ, 470, 35

de Vaucouleurs G., de Vaucouleurs A., Corwin Jr. H.G., Buta R.J., Paturel G., &Fouque P., 1991, Third Reference
    Catalogue of Bright Galaxies (RC3 Catalog)

Eskridge, P.B., Fabbiano, G., and Kim, D.-W., 1995, ApJ, 97, 141

Edge, A.C., & Stewart, G.C., 1991, MNRAS, 252, 414

Faber, S.M., Wegner, G., Burstein, D., Davies, R.L., Dresller, A., Lynden-Bell, D., Terlevich, R.J. 1989 ApJS, 69,763

Fabbiano, G., 1989, ARA&A, 27,87

Fabbiano, G., Gioia, I.M., Trinchieri, G., 1988, ApJ, 324, 749

Fabbiano, G., Kim, D.-W., &,Trinchieri, G. 1992, ApJS, 80, 531

Fabbiano, G., Kim, D.-W., &,Trinchieri, G., 1994, ApJ, 429, 94

Fabian, A.C., Arnaud, K.A., Bautz, M.W., & Tawara, Y. 1994, ApJ, 436, L63

Forman, W., Jones, C., & Tucker, W. 1985, ApJ, 293, 102

Forman, W., Jones, C., David, L., Franx, M., Makishima, K., & Ohashi, T. 1993, ApJL, 418, 55

Fujita, K. et al. 1997, Ph. D. thesis, University of Kyoto

Fukazawa, Y. et al. 1994, PASJ, 46, L141

Fukazawa, Y. et al. 1998, PASJ, 50, 187

Hatsukade, I., 1989, Ph.D. Thesis, Osaka University

Ikebe, Y., et al. 1992, ApJ, 384, L5

Ikebe, Y., et al. 1996, Nature, 379, 427

Ikebe Y., et al. 1999, ApJ, 525, 581

Ishiamaru Y., 1997, Ph.D. thesis, University of Tokyo

Ishisaki Y., 1996, Ph.D. thesis, University of Tokyo

Itoh, H. 1989, PASJ, 41, 853

Kaastra, J.S. 1992, An X-Ray Spectral Code for Optically Thin Plasmas (Internal SRON-Leiden Report, updated
    version 2.0)

Kobayashi C., and Arimoto N., 1999, accepted to ApJ

Kodama, K., and Matsushita, K., 2000, submitted to ApJ

Liedahl, D. A., Osterheld, A.L., & Goldstein, W.H. 1995, ApJ, 438, L115

Loewenstein, M., & Mathews, W.G. 1991, ApJ, 373, 445

Loewenstein, M., Mushotzky, R., Tamura, T., Ikebe, Y., Makishima, K., Matsushita, K., Awaki, H., & Serlemitsos, P.
    1994, ApJL, 436, 75

Makishima, K. et al. 1996, PASJ, 48, 171

Masai, K. 1984,Ap&SS, 98, 367

Masai, K. 1997, A&A, 324, 410

Matsumoto, H., Koyama, K., Awaki, H., Tsuru, T., Loewenstein, M., & Matsushita, K. 1997, ApJ, 482, 133

Matsushita, K. et al. 1994, ApJL, 436, 41

Matsushita, K. 1997, Ph.D. thesis, University of Tokyo

Matsushita, K., Makishima, K., Rokutanda, E., Yamasaki, N., & Ohashi, T., 1997, ApJ, 488, 125

Matsushita, K., Makishima, K., Ikebe, Y., Rokutanda, E., Yamasaki, N., & Ohashi, T., 1998, ApJL, 499, 13

Matsushita, K, 2000, submitted to ApJ

Mewe, R., Gronenschild, E.H.B.M., & van den Oord, G.H.J. 1985, A&AS, 62,197

Mewe, R., Lemen, J.R., & van den Oord, G.H.J. 1986, A&AS, 65,511

Mushotzky, R.F., Loewenstein, M., Awaki, H., Makishima, K., Matsushita, K., & Matsumoto, H. 1994, ApJL, 436, 79

Ohashi, T. et al. 1996, PASJ, 48, 157

Raymond, J.C., & Smith, B.W. 1977, ApJS, 35, 419

Renzini, A., Ciotti, L., D'Ercole, A., & Pellegrini, S. 1993, ApJ, 419, 52

Sadler, E.M., Jenkins, C. R., & Kotanyi, C.G., 1989, MNRAS, 240, 591

Serlemitsos, P.J., Loewenstein, M., Mushotzky, R.F., Marshall, F.E, & Petre, R. 1993, ApJ, 413, 518

Tammann, G., & Sandage, A., 1995, ApJ, 452, 16

Thielemann, F-K., Nomoto, K., & Hashimoto, M. 1996, ApJ, 460, 408

Trinchieri, G., Fabbiano, G., & Canizares, C.R., 1986, ApJ, 310, 637

Trinchieri, G., Kim, D.-W., Fabbiano, G., & Canizares, C.R. 1994, ApJ, 428, 555

Trinchieri, G., Fabbiano, G. and Kim, D.-W., 1997, A&A, 318, 361

Tsuru, T. 1993, PhD Thesis, University of Tokyo, ISAS RN 528

Tully, R.B., 1988, Nearby Calaxies Catalog, Cambridge: Cambridge University Press)

van den Bergh, S., & Tammann, G. 1991, ARA&A, 29, 363

Whitemore, B.C., McElroy, D.B., & Tonry, J.L., 1985, ApJS, 59, 1

Worthey, G., Faber, S.M., & González, J.J. 1992, ApJ, 398, 69
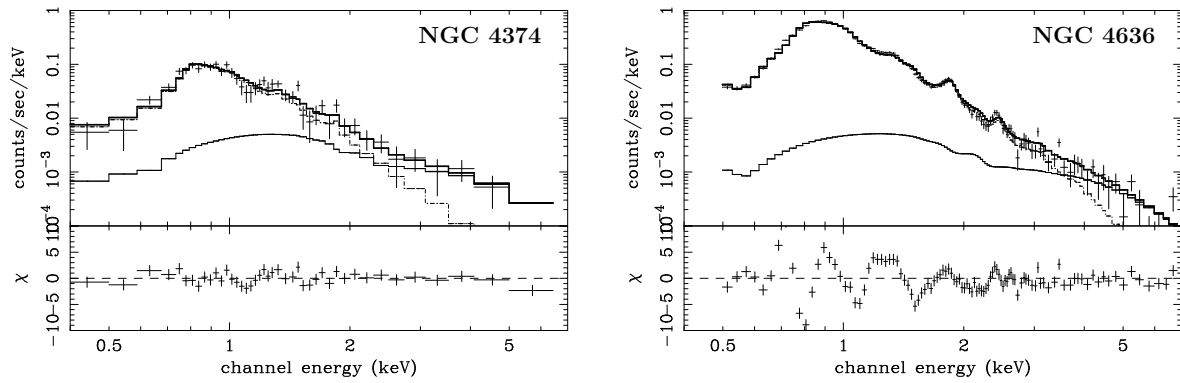
Fig. 1. The SIS spectra (crosses) of (a) NGC 4374 and (b) NGC 4636 fitted with the double-component model, consisting of a soft R-S component (dot-dash line) and a hard bremsstrahlung component (thin solid line). The bottom panels show residuals of the fit.
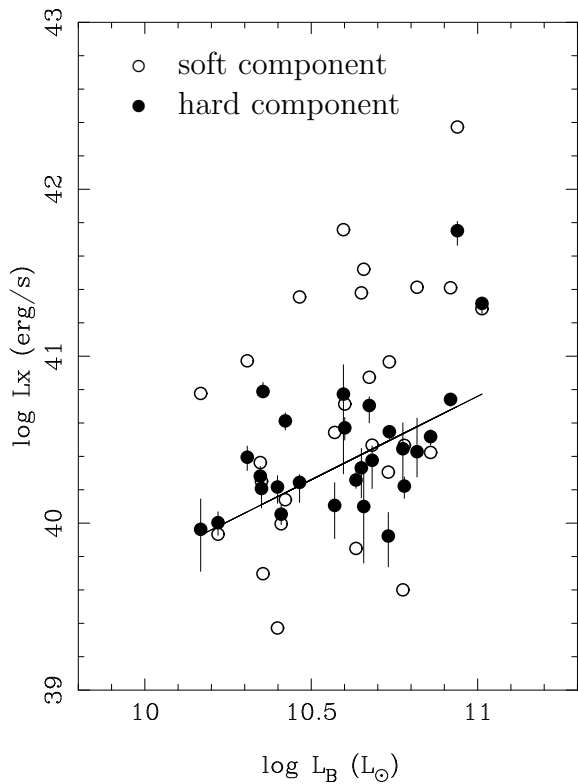
Fig. 2. X-ray (0.5–10.0 keV) vs. B-band luminosities of early-type galaxies. Open and closed circles represent the soft and hard components, respectively. Solid line represents the contribution of discrete sources estimated by Canizares et al. (1987) from X-ray luminosities of bulges of early spiral galaxies.
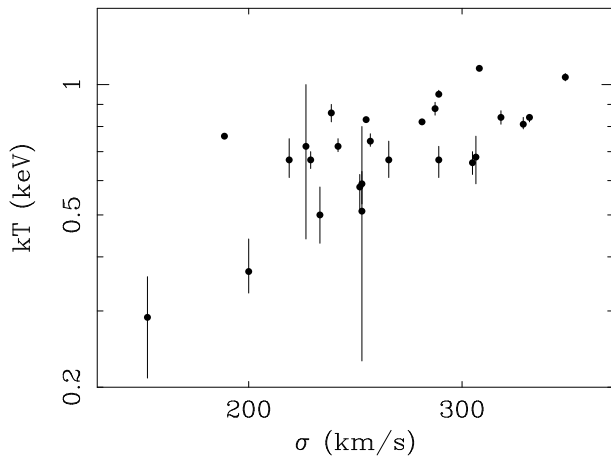
Fig. 3.   The ISM temperature vs. the central stellar velocity dispersion (σ) of the galaxies.

1
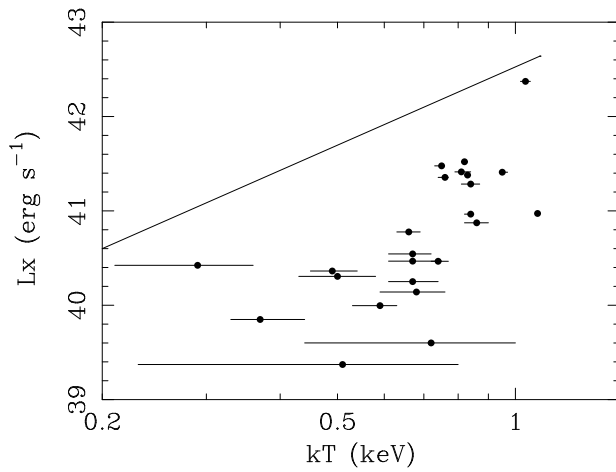
Fig. 4. The X-ray luminosities vs. temperature of the ISM (filled circles). The solid line represents an extrapolation

of the average kT vs. L_X (bolometric) relation for clusters of galaxies (Edge et al. 1991).
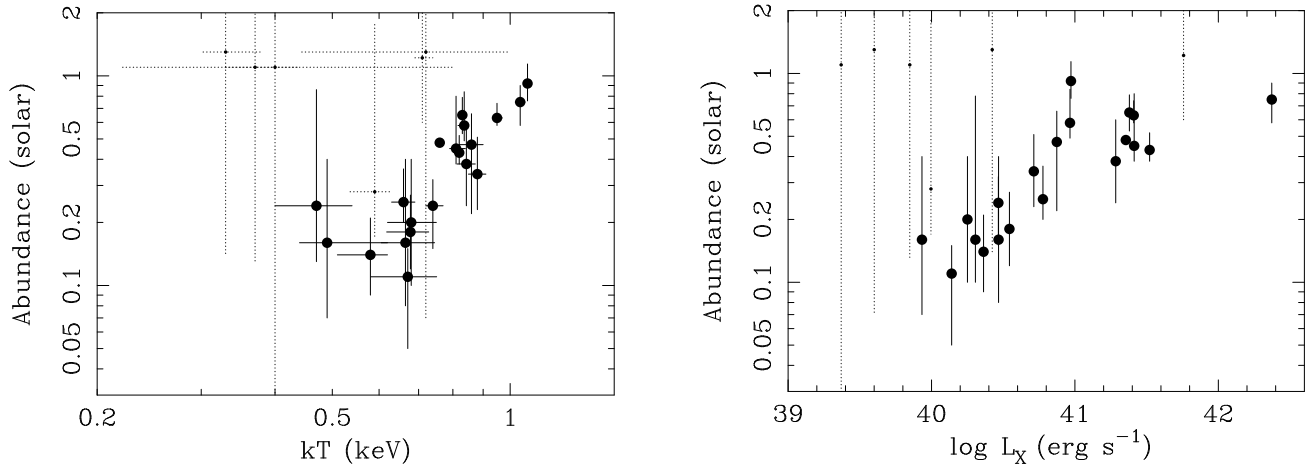
Fig. 5. (a) The abundance vs. temperature of the ISM. We show the data with large uncertainty (relative error exceeding 50%) in dotted lines in order to highlight the high-quality data points. (b) The abundance vs. ISM luminosity (0.5–10.0 keV; $r < 4r_e$).
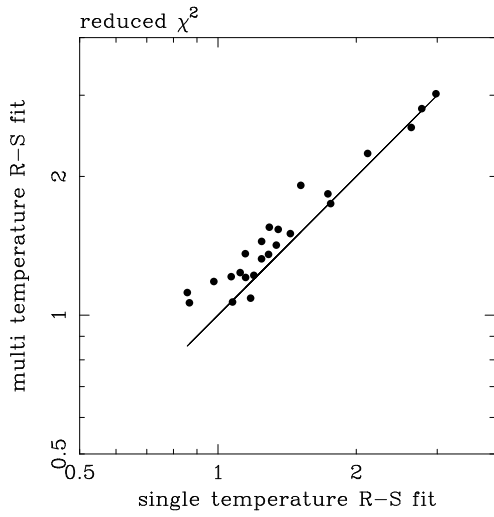
Fig. 6.　Comparison of the reduced χ^2 between the 1 temperature R-S + bremsstrahlung fit vs. multi-temperature R-S + bremsstrahlung fit. Solid line indicates the equal value between the two fits.
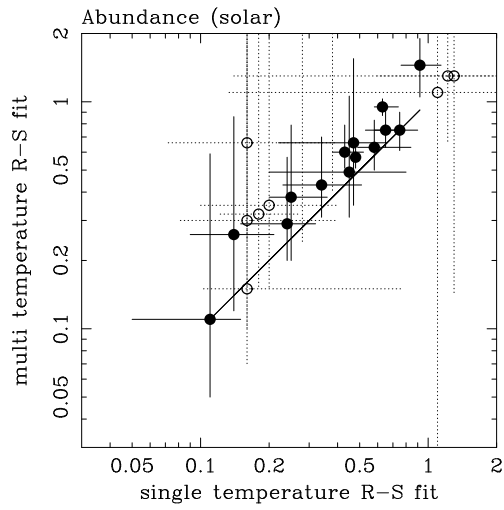
Fig. 7.   Comparison of the derived abundances between the 1 temperature R-S + bremsstrahlung fit vs. multi-
temperature R-S + bremsstrahlung fit. Solid line indicates the equal value between the two fits. In order to
emphasize the high quality data, the points with large error bars are represented in dotted lines.
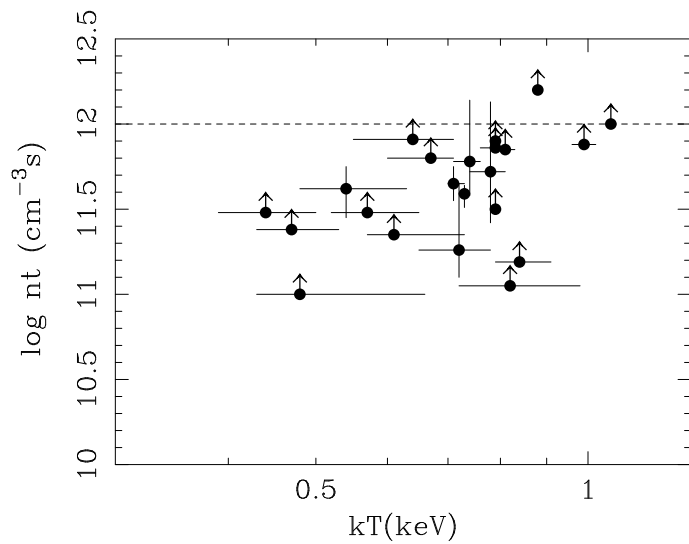
Fig. 8.   nt vs. the ISM temperature derived from the NEI Masai model.
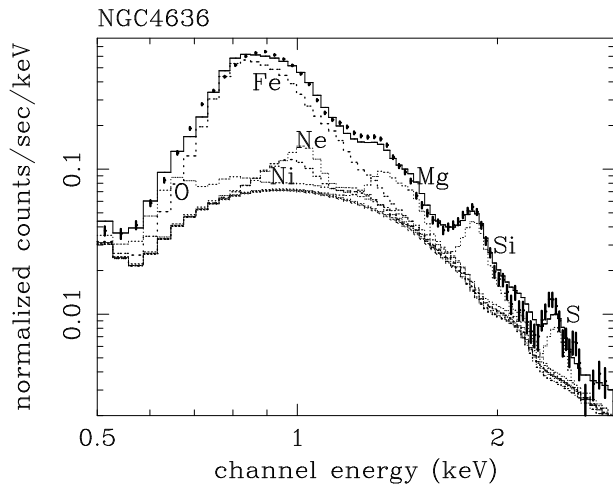
Fig. 9. The SIS spectrum of NGC 4636 and the best-fit model prediction, decomposed into contributions from

individual elements.
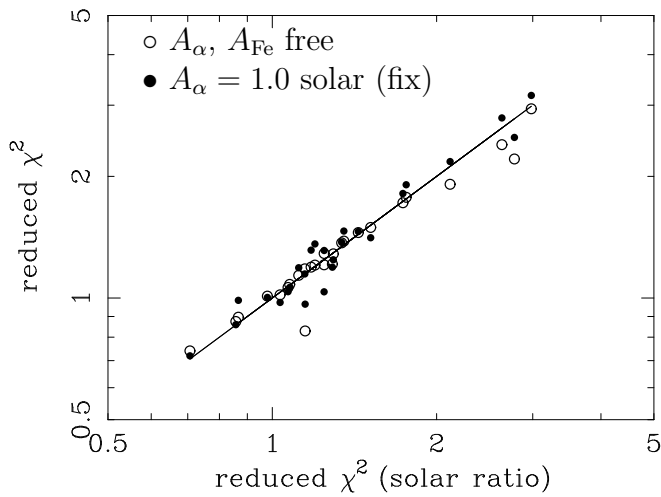
Fig. 10.   Reduced χ^2 derived with A_α and A_{Fe} allowed to be separate (open circles) or asuming A_α =1.0 solar

(closed circles), plotted in the ordinate, against those derived assuming solar abundance ratio in the abscissa.
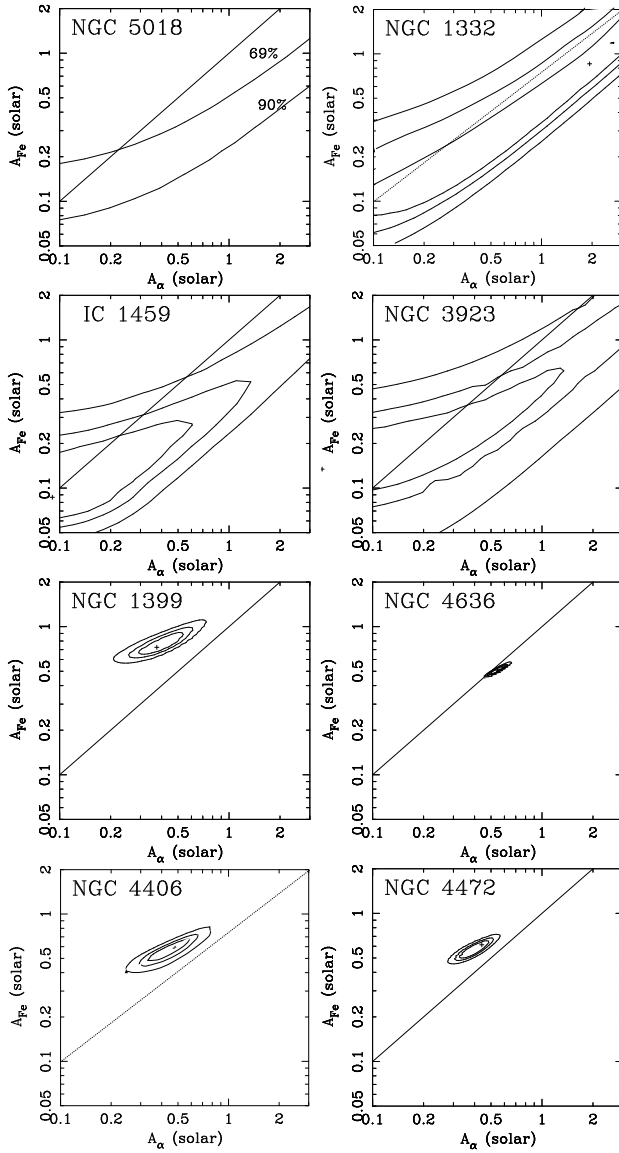
Fig. 11.   Confidence contours (69%, 90%, and 99%) for $A_{\rm Fe}$ vs. A_α for the ISM of representative early-type galaxies,

obtained with the R-S model. Solid lines indicate the condition of solar abundance ratio. The area of confidence

regions is heavily under-estimated for X-ray luminous galaxies because their fits are not formally acceptable.
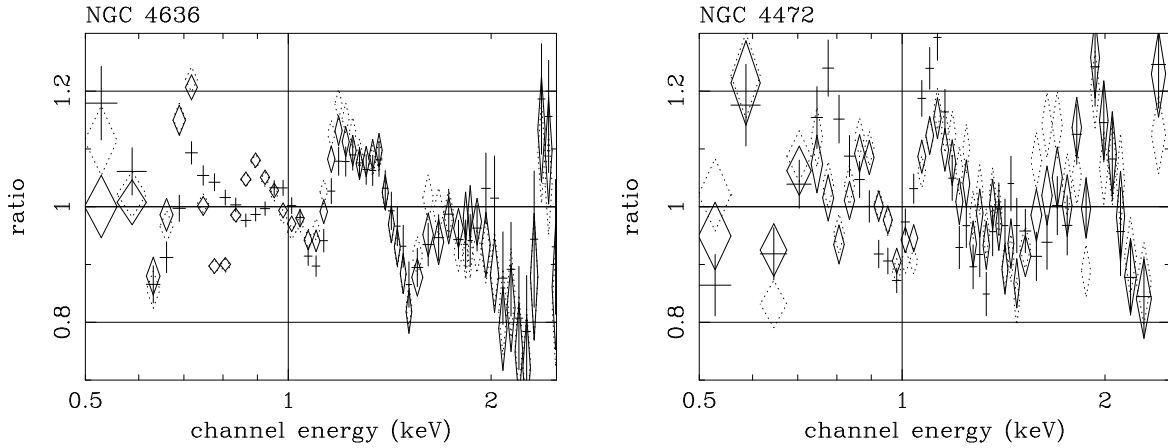
Fig. 12.   The data-to-model ratio of the SIS spectra of NGC 4636 (observed in AO5) and NGC 4472. Abundances of heavy elements are grouped into α-elements and iron group. The solid diamonds represent the fit allowing both A_α and $A_{\rm Fe}$ to be free, and dotted diamonds represent the model fixing A_α to be 1.0 solar. Those for the best fit MEKAL model (both A_α and $A_{\rm Fe}$ are allowed to be free) are also shown (crosses).
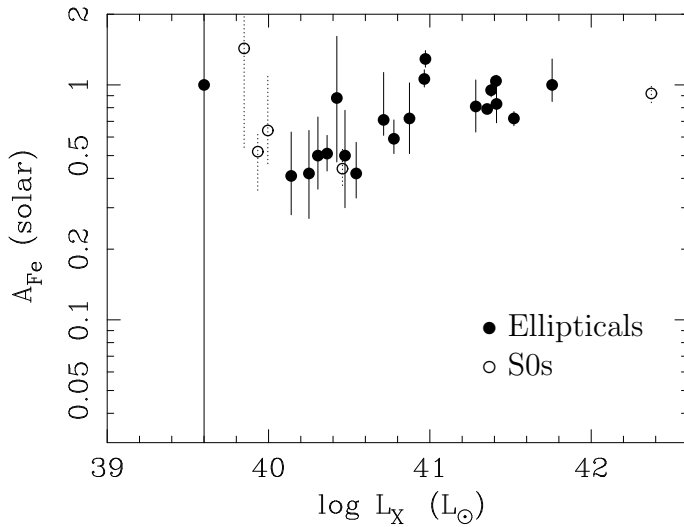
Fig. 13. $A_{\rm Fe}$ vs. ISM luminosity (0.5-10.0 keV) within $r < 4r_e$ when A_α is fixed to 1.0 solar. Open circles indicate S0 galaxies, and filled circles are elliptical galaxies.
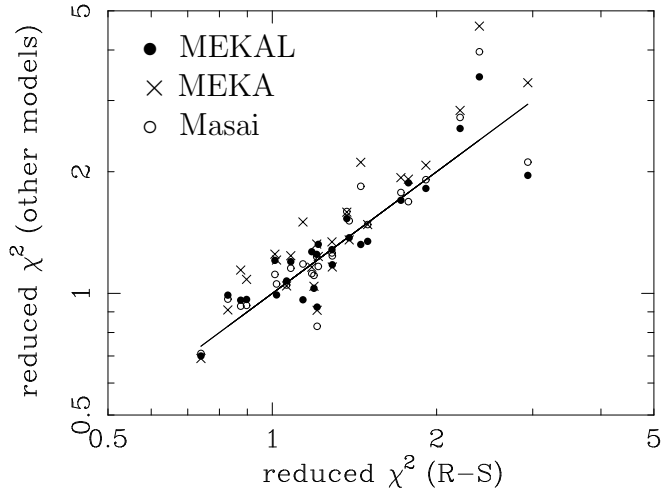
Fig. 14.   The reduced χ^2 of the spectral fits, obtained by MEKAL (closed circle), MEKA (crosses), and Masai (open circles) codes, plotted against those obtained by the R-S model.
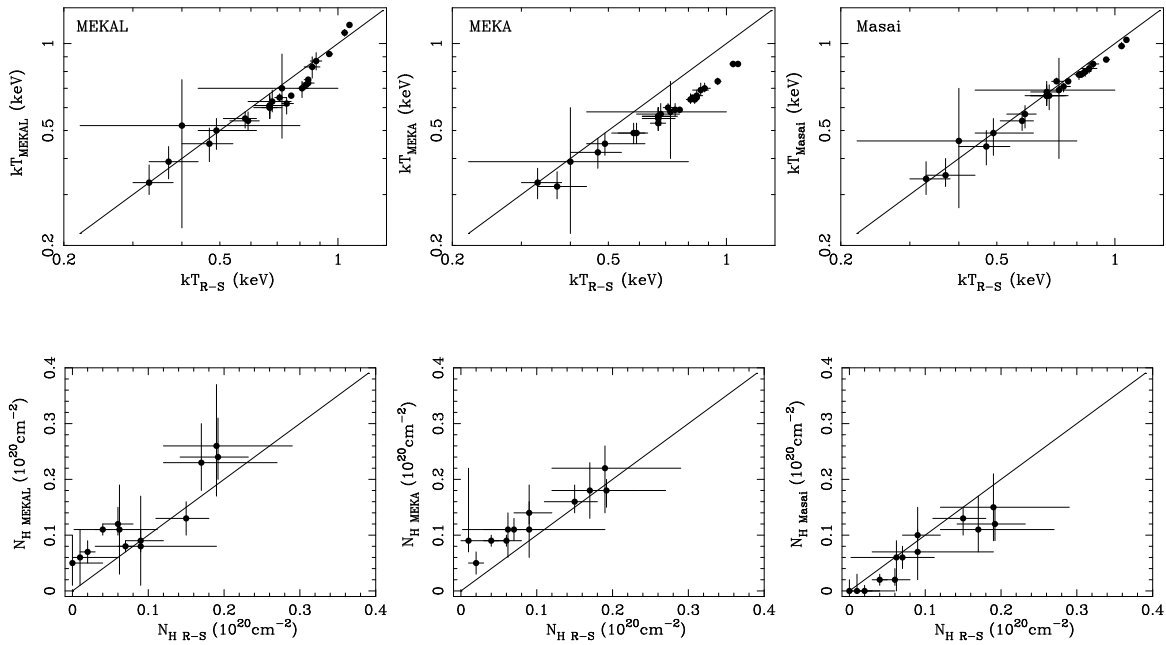
Fig. 15.   The results from the MEKAL, MEKA, and Masai model fits, shown against those obtained with the R-S model for (a) temperature and (b) hydrogen column density.
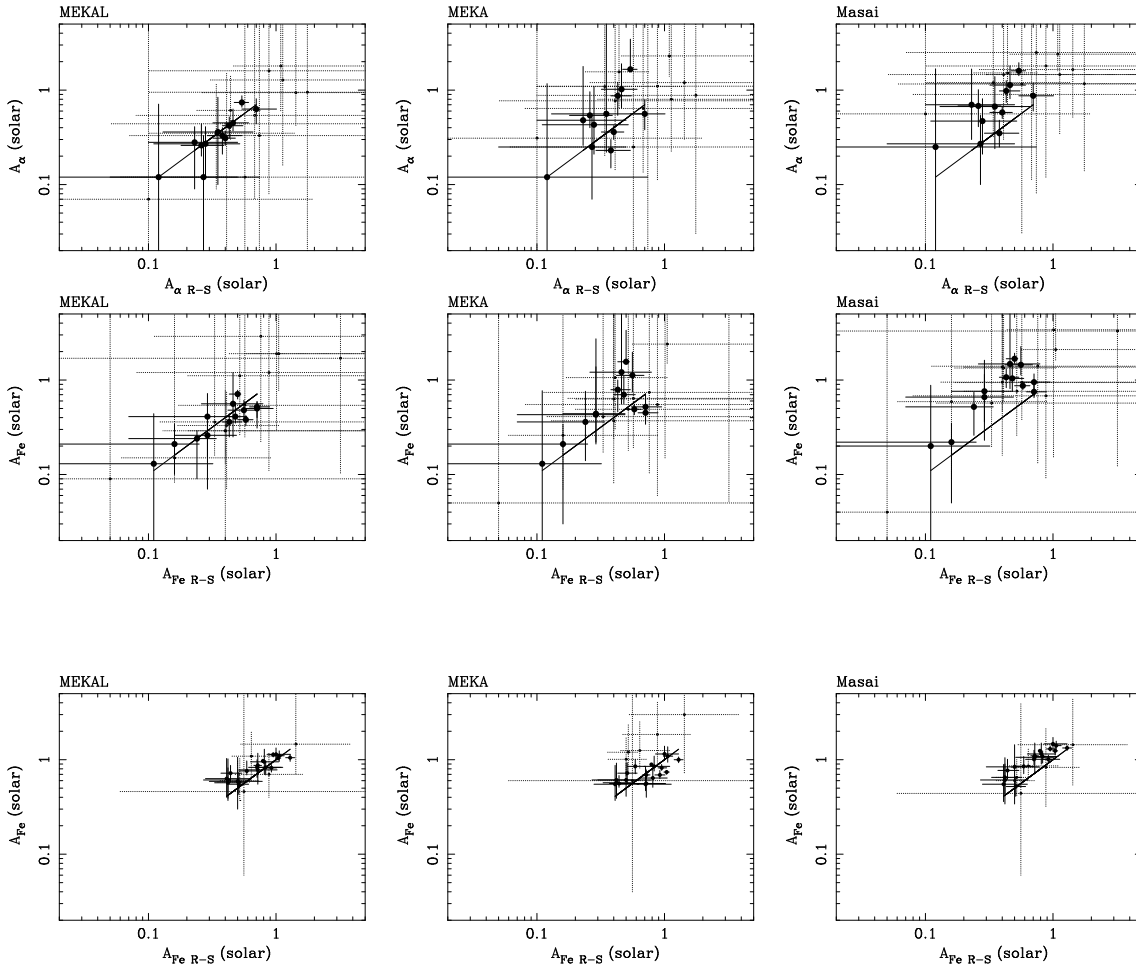
Fig. 16.   The abundances derived by MEKAL, MEKA, and Masai models, shown against those obtained with the R-S model. In order to emphasize the high quality data, the points with large error bars are represented in dotted lines. (a) Both A_α and A_{Fe} are allowed to be free. (b) A_α is fixed to be 1 solar, and A_{Fe} is plotted.
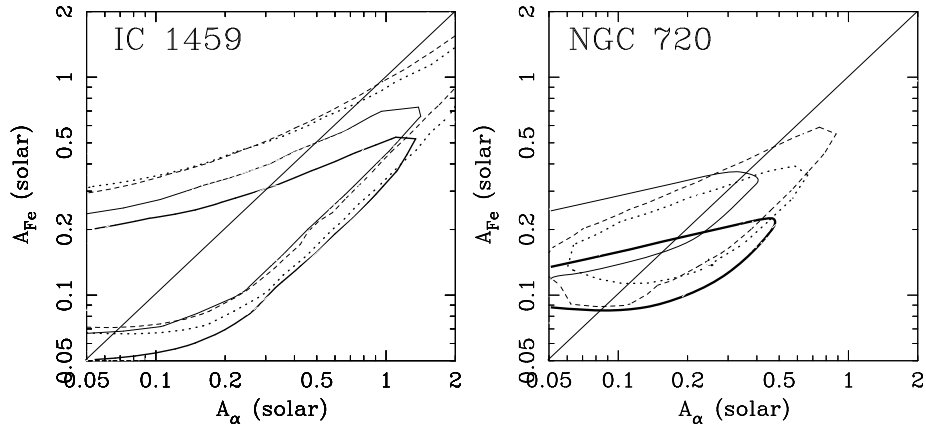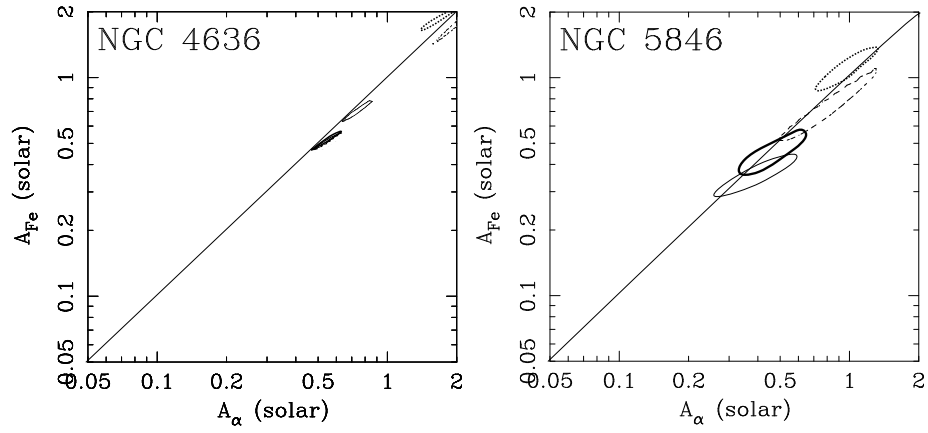
Fig. 17.   90 % confidence contours of the correlation between $A_{\rm Fe}$ vs. A_α for four galaxies, obtained by R-S (thick-solid), MEKA (dashed), MEKAL (thin-solid), and Masai (dotted) models.
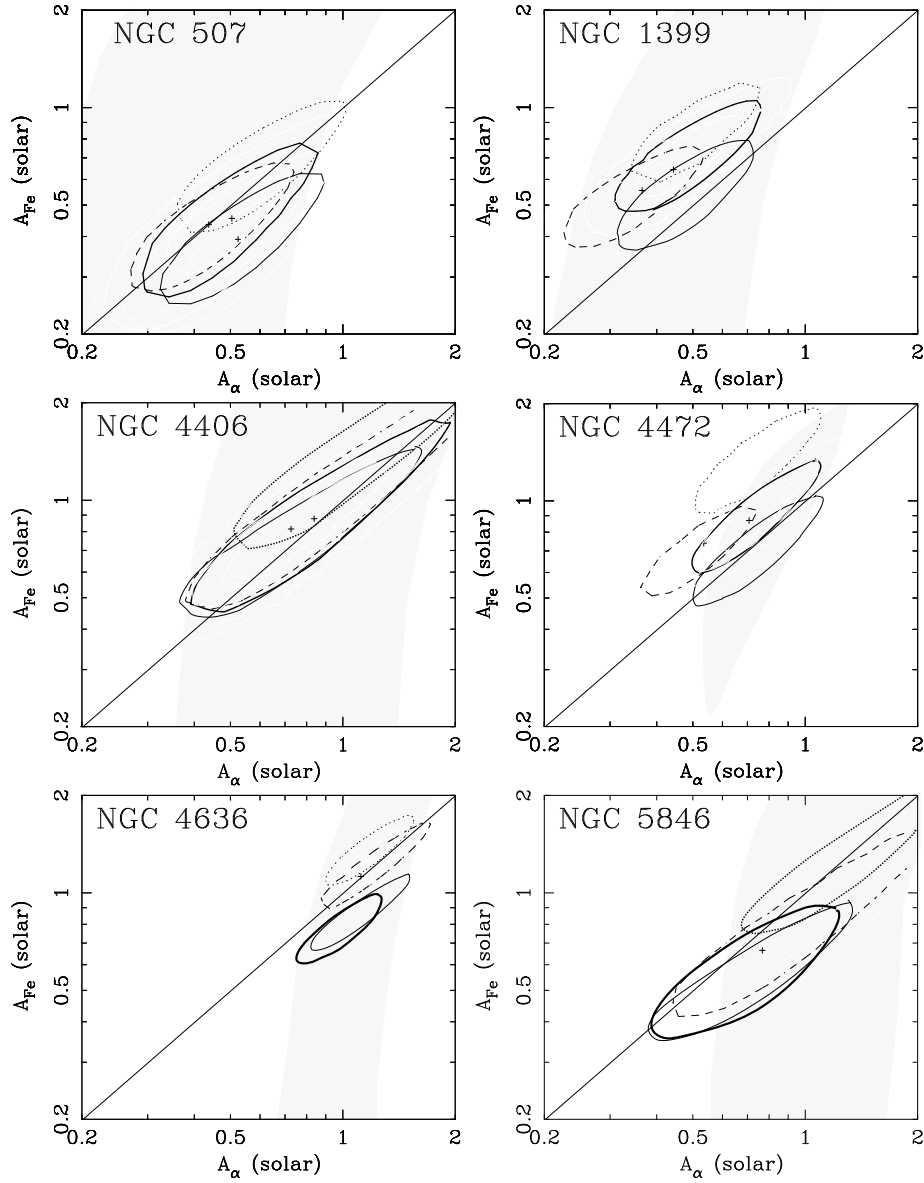
Fig. 18. Confidence regions (90%) of A_{Fe} vs. A_{α} obtained by fitting the spectra only above 1.6 keV (SIS) and 1.7 keV (GIS), using the R-S model (shaded region). Contours show the results obtained by R-S (solid), MEKAL (thin), MEKA (dash) and Masai (dot) models, when 20 % systematic errors are included in the energy range of 0.4–1.6 keV.
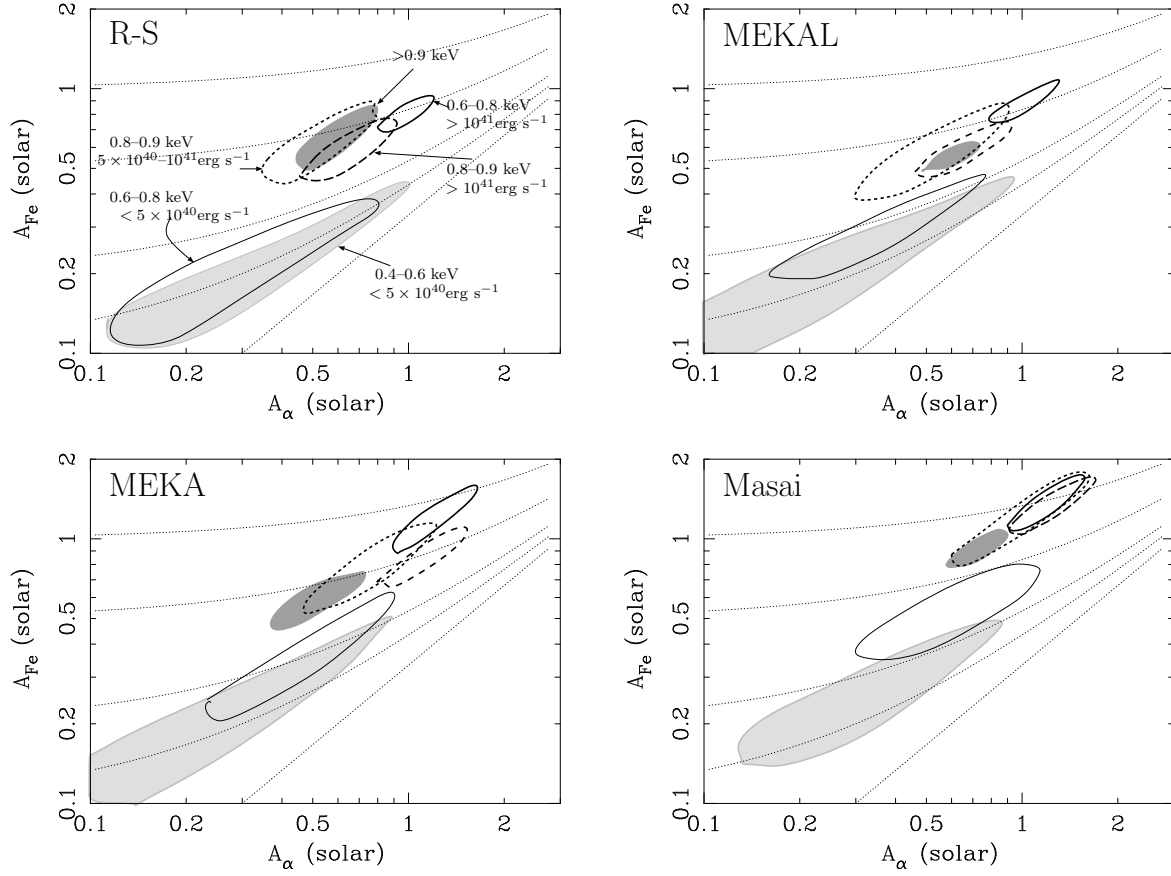
Fig. 19. Confidence contours of A_α vs A_{Fe} of galaxies. Galaxies are allocated into 6 groups: $kT > 0.9$ keV (hatched region), $0.8 < kT < 0.9$ keV and $L_X > 10^{41}$erg s^{-1} (dased lines), $0.8 < kT < 0.9$ keV and $5 \times 10^{40} < L_X < 10^{41}$erg s^{-1} (dotted lines), $0.6 < kT < 0.8$ keV and $L_X > 10^{41}$erg s^{-1} (bold lines), $0.6 < kT < 0.8$ keV and $L_X < 5 \times 10^{40}$erg s^{-1} (thin lines), and $0.4 < kT < 0.6$ keV and $L_X < 5 \times 10^{40}$erg s^{-1} (dotted region). Each dotted curve traces the abundance change when contribution from SN II is varied with a fixed SN Ia imput. Different curves, on the other hand, correspond to the change in the SN Ia contribution.
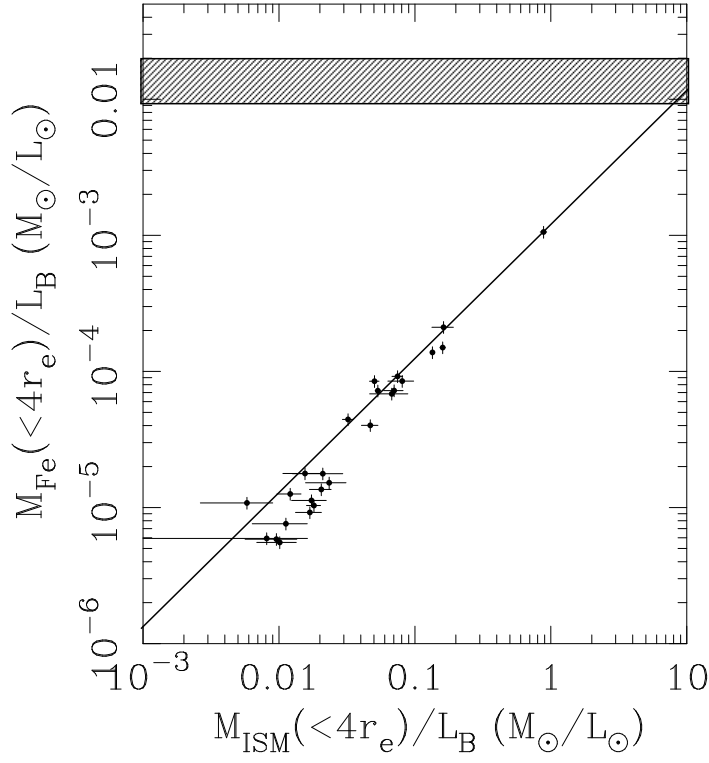
Fig. 20. The ratio $M_{\mathrm{Fe}}(R < 4r_e)/L_B$ (IMLR) are plotted against $M_{\mathrm{ISM}}(R < 4r_e)/L_B$. The hatched region represents the IMLR for clusters. The solid line represents the relation of IMLR $\propto M_{\mathrm{ISM}}(R < 4r_e)/L_B$ whch fits the data for X-ray luminous objects.

Table 1.   The sample

galaxy	(1)	B (2)	D (3)	L_B (4)	σ (5)	r_e (6)	L_X (7)
NGC 499	-3	12.79	68.0	10.60	237	21	42.20
NGC 507	-2	12.19	68.0	10.94	365	77	42.69
NGC 720	-5	11.15	20.3	10.34	247	40	40.93
NGC 1316	-2	9.67	16.9	10.78	252*	81	40.83
NGC 1332	-2	11.17	17.7	10.22	306*	28*	40.40
NGC 1399	-5	10.85	16.9	10.31	310	42	41.90
NGC 1404	-5	11.20	16.9	10.17	225	27	41.06
NGC 1407	-5	10.65	21.6	10.60	285	72	40.90
NGC 3607	-2	10.95	19.9	10.41	248	66	40.47
NGC 3923	-5	10.83	25.8	10.68	216	53	40.94
NGC 4125	-5	10.57	24.2	10.73	229	60	——
NGC 4365	-5	10.61	16.8	10.40	248	57	40.01
NGC 4374	-5	10.18	16.8	10.57	287	55	40.75
NGC 4382	-2	10.02	16.8	10.64	200*	55*	40.31
NGC 4406	-5	9.98	16.8	10.65	250	91	41.83
NGC 4472	-5	9.31	16.8	10.92	287	104	41.65
NGC 4552	-5	10.73	16.8	10.35	261	30	40.51
NGC 4636	-5	10.47	17.0	10.46	191	102	41.58
NGC 4649	-5	9.77	16.8	10.74	341	74	41.20
NGC 4697	-5	10.17	23.3	10.85	165	75	40.56
NGC 5018	-6	11.60	40.9	10.78	223	25	——
NGC 5084	-2	11.70	26.4	10.36	213*	51*	40.80
NGC 5846	-5	11.11	28.5	10.66	278	83	41.70
NGC 7619	-5	11.93	49.9	10.82	337	32	41.65
NGC 7626	-5	12.06	49.9	10.67	234	38	41.23
IC 1459	-5	10.93	20.0	10.42	308	39	40.60
IC 4296	-5	11.42	53.4	11.01	323	57	41.63

Column (1) :   Morphology (RSA) -2: S0; -5: E

Column (2) :   Total B band magnitude (RC3)

Column (3) :   Distance (Mpc) (Tully 1988)

Column (4) :   B band luminosity ($L_\odot$) (Tully 1988)

Column (5) :   stellar velocity dispersion at galaxy center (km/s) (Faber et al. 1989), *: Whitemore et al. 1985

Column (6) :   effective radius (arcsec) (Faber et al. 1989), *: RC 3 Catalog

Column (7):   X-ray luminosity (0.2-3.5 keV) (Fabbiano 1992) corrected distance using column (3)

Table 2.   Observatinal log.

target	date[a]	GIS		SIS			
		time[b]	counts/s	time[b]	counts/s	mode[c]	clock[d]
NGC 499	95 01 28	32.9	0.024	44.1	0.067	Faint/Faint	2CCD
NGC 499/507	94 01 24	37.1	0.092	32.9	0.21	Faint/Faint	2CCD
NGC 720	93 07 17	34.8	0.009	35.9	0.028	Faint/Bright	4CCD
NGC 1316	94 01 12	33.0	0.023	31.8	0.058	Faint/Faint	2CCD
NGC 1332	95 08 05	50.1	0.005	55.0	0.013	Faint/Faint	1CCD
NGC 1399/1404	93 07 15	17.2	0.090	23.7	0.25	Faint/Bright	4CCD
NGC 1399/1404	93 07 15	15.2	0.080	20.0	0.19	Faint/Bright	4CCD
NGC 1407	95 08 23	30.9	0.028	35.8	0.066	Faint/Faint	1CCD
NGC 3607	96 05 26	59.5	0.007	63.3	0.019	Faint/Faint	2CCD
NGC 3923	94 07 09	35.8	0.009	33.3	0.022	Faint/Bright	4CCD
NGC 4125	95 04 05	36.6	0.005	35.6	0.015	Faint/Faint	2CCD
NGC 4365	93 06 27	23.8	0.009	37.8	0.016	Faint/Bright	4CCD
NGC 4374	93 07 04	20.7	0.016	20.9	0.058	Faint/Faint	2CCD
NGC 4382	94 05 27	37.3	0.007	37.4	0.020	Faint/Faint	2CCD/1CCD[e]
NGC 4406/4374	93 07 03	19.6	0.14	20.5	0.41	Faint/Bright	4CCD
NGC 4472	93 07 04	20.2	0.21	20.5	0.51	Faint/Bright	4CCD
NGC 4472NW	93 06 30	18.5	0.15	18.6	0.38	Faint/Bright	4CCD
NGC 4552	95 06 26	27.1	0.012	29.0	0.030	Faint/Faint	2CCD
NGC 4636	93 06 22	35.7	0.12	38.9	0.42	Faint/Bright	4CCD
NGC 4636	95 12 28	172.2	0.12	215.0	0.31	Faint/Faint	1CCD
NGC 4643	94 06 05	35.8	0.004	34.3	0.008	Faint/Faint	2CCD
NGC 4649	94 01 07	36.8	0.074	39.7	0.14	Faint/Faint	4CCD/2CCD[e]
NGC 4697	94 07 02	25.9	0.010	28.7	0.023	Faint/Faint	2CCD
NGC 5018	96 01 16	28.4	0.002	44.4	0.005	Faint/Faint	1CCD
NGC 5084	95 07 08	35.0	0.011	34.8	0.020	Faint/Faint	2CCD
NGC 5846	94 02 07	39.0	0.068	39.5	0.18	Faint/Bright	4CCD
NGC 7619/7626	95 06 28	56.0	0.015	50.0	0.042	Faint/Faint	2CCD
IC 1459	93 05 19	27.6	0.017	28.5	0.038	Faint/Bright	4CCD
IC 4296	94 02 15	36.7	0.020	38.2	0.046	Faint/Faint	2CCD

a   Observation start date

b   Exposure time (ks)

c   SIS mode. Mode in BIT High/ Mode in Bit Medium

d   CCD clocking mode

e   CCD clocking mode in BIT High/BIT Med

Table 3.   Summary of spectral fits with the two component model, R-S model with solar abundance ratio and a 10 keV Bremstrallung , for early-type galaxies. Errors show 90% confidence limits for a single parameter.

galaxy	single kT (§3.2)						multi kT (§.3.3)		
	kT	Abundance	N_H	$F_X{}^*$	$F_{X\,\mathrm{h}}{}^*$	χ^2/ν	Abundance	N_N	χ^2/ν
	(keV)	(solar)	$(10^{22}\mathrm{cm}^{-2})$	$(10^{-13}\mathrm{ergs}^{-1}\mathrm{cm}^{-2})$			(solar)	$(10^{22}\mathrm{cm}^{-2})$	
NGC 499	$0.71^{+0.03}_{-0.02}$	$1.22^{+3.5}_{-0.62}$	$0.20^{+0.06}_{-0.07}$	16.0	1.5	52.3/61	$1.30\ (>0.71)$	$0.15^{+0.06}_{-0.04}$	62.6/56
NGC 507	$1.04^{+0.02}_{-0.02}$	$0.75^{+0.15}_{-0.17}$	$0.15^{+0.01}_{-0.01}$	58.5	11.3	162.4/113	$0.75^{+0.15}_{-0.14}$	$0.15^{+0.01}_{-0.01}$	162.3/108
NGC 720	$0.58^{+0.04}_{-0.07}$	$0.14^{+0.07}_{-0.05}$	0.01 (fix)	8.6	3.9	35.6/31	$0.26^{+0.60}_{-0.14}$	0.01 (fix)	31.4/26
NGC 1316	$0.74^{+0.03}_{-0.02}$	$0.24^{+0.08}_{-0.09}$	$0.00^{+0.03}_{-0.00}$	13.5	4.9	78.9/67	$0.29^{+0.28}_{-0.09}$	$0.00^{+0.07}_{-0.00}$	67.5/62
NGC 1332	$0.49^{+0.13}_{-0.05}$	$0.16^{+0.24}_{-0.09}$	0.02 (fix)	5.0	2.7	31.8/21	$0.66\ (>0.22)$	0.02 (fix)	30.6/16
NGC 1399	$1.07^{+0.01}_{-0.01}$	$0.92^{+0.22}_{-0.16}$	$0.07^{+0.02}_{-0.01}$	34.9	7.3	202.7/73	$1.45^{+0.45}_{-0.40}$	$0.08^{+0.01}_{-0.01}$	190.8/68
NGC 1404	$0.67^{+0.03}_{-0.03}$	$0.25^{+0.11}_{-0.05}$	$0.02^{+0.04}_{-0.02}$	17.0	2.7	56.8/42	$0.38^{+0.45}_{-0.19}$	$0.02^{+0.11}_{-0.02}$	56.8/37
NGC 1407	$0.88^{+0.03}_{-0.03}$	$0.34^{+0.17}_{-0.11}$	$0.10^{+0.08}_{-0.07}$	16.0	6.7	76.6/64	$0.43^{+0.27}_{-0.12}$	$0.10^{+0.08}_{-0.06}$	72.0/59
NGC 3607	$0.59^{+0.04}_{-0.06}$	$0.28^{+1.52}_{-0.11}$	0.02 (fix)	4.5	2.4	62.4/58	$2.40\ (>0.24)$	0.02 (fix)	56.6/53
NGC 3923	$0.67^{+0.08}_{-0.06}$	$0.16^{+0.24}_{-0.08}$	0.06 (fix)	6.7	3.0	33.6/27	$0.30\ (>0.10)$	0.06 (fix)	31.8/22
NGC 4125	$0.47^{+0.07}_{-0.07}$	$0.24^{+0.62}_{-0.11}$	0.02 (fix)	4.4	1.6	31.1/25	$0.15\ (>0.08)$	0.02 (fix)	26.5/20
NGC 4365	$0.40^{+0.40}_{-0.18}$	$1.1\ (>0.0)$	0.02 (fix)	5.6	4.9	21.9/31	$1.1\ (>0.0)$	0.02 (fix)	21.9/26
NGC 4374	$0.67^{+0.05}_{-0.06}$	$0.18^{+0.09}_{-0.06}$	$0.10^{+0.04}_{-0.03}$	14.2	3.8	77.3/60	$0.32\ (>0.15)$	$0.10^{+0.04}_{-0.08}$	74.5/55
NGC 4382	$0.37^{+0.07}_{-0.04}$	$1.1\ (>0.13)$	0.03 (fix)	7.5	5.4	38.8/30	$1.1\ (>0.03)$	0.03 (fix)	38.8/25
NGC 4406	$0.83^{+0.01}_{-0.01}$	$0.65^{+0.14}_{-0.12}$	$0.07^{+0.02}_{-0.02}$	77.7	6.38	249.8/144	$0.75^{+0.23}_{-0.12}$	$0.08^{+0.03}_{-0.03}$	254.8/139
NGC 4472	$0.95^{+0.02}_{-0.01}$	$0.63^{+0.11}_{-0.05}$	$0.05^{+0.02}_{-0.08}$	92.9	16.4	466.2/177	$0.95^{+0.08}_{-0.08}$	$0.06^{+0.02}_{-0.01}$	439.3/172
NGC 4552	$0.67^{+0.07}_{-0.06}$	$0.20^{+0.20}_{-0.10}$	0.03 (fix)	10.1	4.8	40.6/38	$0.35\ (>0.15)$	0.03 (fix)	40.0/33
NGC 4636	$0.76^{+0.01}_{-0.01}$	$0.48^{+0.02}_{-0.02}$	$0.05^{+0.01}_{-0.01}$	70.9	5.1	1112/373	$0.58^{+0.05}_{-0.05}$	$0.05^{+0.01}_{-0.01}$	1112/368
NGC 4649	$0.84^{+0.01}_{-0.02}$	$0.58^{+0.26}_{-0.09}$	$0.12^{+0.05}_{-0.02}$	38.0	10.5	243.4/115	$0.63^{+0.20}_{-0.13}$	$0.12^{+0.04}_{-0.03}$	246.7/110
NGC 4697	$0.33^{+0.05}_{-0.03}$	$1.3\ (>0.14)$	0.02 (fix)	9.2	5.1	36.7/32	$1.3\ (>0.14)$	0.02 (fix)	36.7/27
NGC 5018	$0.72^{+0.28}_{-0.28}$	$1.3\ (>0.07)$	0.07 (fix)	1.6	1.4	12.4/12	$1.3\ (>0.07)$	0.07 (fix)	12.4/7
NGC 5084	0.70 (fix)	0.3 (fix)	0.08 (fix)	8.0	7.4	50.5/29	2.0 (>0.0)	0.08 (fix)	50.5/24
NGC 5846	$0.82^{+0.01}_{-0.01}$	$0.43^{+0.09}_{-0.05}$	$0.02^{+0.01}_{-0.13}$	35.6	1.3	212.8/121	$0.60^{+0.20}_{-0.13}$	$0.06^{+0.04}_{-0.03}$	202.5/116
NGC 7619	$0.81^{+0.03}_{-0.02}$	$0.45^{+0.35}_{-0.07}$	$0.24^{+0.07}_{-0.06}$	9.6	0.9	57.0/51	$0.49^{+0.57}_{-0.18}$	$0.21^{+0.05}_{-0.05}$	56.9/46
NGC 7626	$0.86^{+0.04}_{-0.04}$	$0.47^{+0.19}_{-0.25}$	0.06 (fix)	5.2	2.1	28.4/29	$0.66^{+0.89}_{-0.31}$	0.06 (fix)	28.4/24
IC 1459	$0.68^{+0.08}_{-0.09}$	$0.11^{+0.04}_{-0.06}$	0.01 (fix)	11.5	8.6	26.0/30	$0.11^{+0.48}_{-0.06}$	0.01 (fix)	26.6/25
IC 4296	$0.84^{+0.03}_{-0.03}$	$0.38^{+0.22}_{-0.14}$	0.04 (fix)	13.7	7.1	71.0/53	$1.27\ (>0.37)$	0.04 (fix)	68.1/48

*: X-ray flux (0.5-10.0 keV). h means hard component.

Table 4.   Summary of spectral fits with variable abundance R-S model.

galaxy	varying A_α and A_{Fe}					A_α=1.0 solar (fixed)			
	kT	A_α	A_{Fe}	N_H	χ^2/ν	kT	A_{Fe}	N_H	χ^2/ν
	(keV)	(solar)	(solar)	(10^{22}cm^{-2})		(keV)	(solar)	(10^{22}cm^{-2})	
NGC 499	$0.72^{+0.03}_{-0.03}$	$1.09(>0.46)$	$1.05(>0.56)$	$0.17^{+0.10}_{-0.05}$	52.5/60	$0.72^{+0.03}_{-0.03}$	$1.00^{+0.29}_{-0.15}$	$0.18^{+0.09}_{-0.05}$	52.4/61
NGC 507	$1.04^{+0.03}_{-0.02}$	$0.70^{+0.31}_{-0.16}$	$0.71^{+0.24}_{-0.14}$	$0.15^{+0.03}_{-0.04}$	162.6/112	$1.05^{+0.02}_{-0.02}$	$0.92^{+0.09}_{-0.08}$	$0.14^{+0.03}_{-0.03}$	165.0/113
NGC 720	$0.53^{+0.10}_{-0.05}$	$0.27^{+0.23}_{-0.22}$	$0.16^{+0.09}_{-0.06}$	0.01 (fix)	25.7/31	$0.60^{+0.05}_{-0.10}$	$0.51^{+0.10}_{-0.08}$	0.01 (fix)	30.9/32
NGC 1316	$0.74^{+0.04}_{-0.05}$	$0.28^{+0.24}_{-0.17}$	$0.24^{+0.10}_{-0.08}$	$0.00^{+0.04}_{-0.00}$	78.7/66	$0.70^{+0.04}_{-0.04}$	$0.44^{+0.10}_{-0.07}$	$0.00^{+0.02}_{-0.00}$	88.0/67
NGC 1332	$0.48^{+0.09}_{-0.08}$	$1.76(>0.10)$	$0.88(>0.08)$	0.02 (fix)	29.9/20	$0.48^{+0.07}_{-0.07}$	$0.52^{+0.10}_{-0.17}$	0.02 (fix)	29.6/21
NGC 1399	$1.08^{+0.01}_{-0.01}$	$0.38^{+0.16}_{-0.09}$	$0.71^{+0.18}_{-0.02}$	$0.09^{+0.03}_{-0.02}$	159.0/72	$1.09^{+0.01}_{-0.01}$	$1.29^{+0.11}_{-0.10}$	$0.07^{+0.02}_{-0.02}$	182.2/73
NGC 1404	$0.67^{+0.03}_{-0.04}$	$0.35^{+0.31}_{-0.22}$	$0.29^{+0.20}_{-0.09}$	$0.01^{+0.05}_{-0.01}$	56.7/41	$0.67^{+0.02}_{-0.02}$	$0.59^{+0.12}_{-0.08}$	$0.00^{+0.03}_{-0.00}$	61.5/42
NGC 1407	$0.88^{+0.03}_{-0.03}$	$0.23^{+0.27}_{-0.13}$	$0.29^{+0.20}_{-0.09}$	$0.09^{+0.10}_{-0.06}$	76.0/63	$0.88^{+0.02}_{-0.05}$	$0.71^{+0.42}_{-0.10}$	$0.10^{+0.19}_{-0.05}$	87.1/64
NGC 3607	$0.58^{+0.05}_{-0.05}$	$0.57(>0.06)$	$0.40(>0.13)$	0.02 (fix)	61.6/57	$0.58^{+0.05}_{-0.05}$	$0.64^{+0.46}_{-0.19}$	0.02 (fix)	61.6/58
NGC 3923	$0.67^{+0.08}_{-0.08}$	$0.10^{+1.87}_{-0.10}$	$0.16^{+0.75}_{-0.08}$	0.06 (fix)	33.5/26	$0.67^{+0.07}_{-0.08}$	$0.50^{+0.28}_{-0.20}$	0.06 (fix)	35.4/27
NGC 4125	$0.46^{+0.06}_{-0.05}$	$1.13(>0.30)$	$0.52(>0.20)$	0.02 (fix)	29.0/24	$0.45^{+0.06}_{-0.04}$	$0.50^{+0.23}_{-0.14}$	0.02 (fix)	25.9/25
NGC 4365	$0.38^{+0.41}_{-0.24}$	$0.00(>0.00)$	$0.05(>0.2)$	0.02 (fix)	22.2/30	$0.36^{+0.41}_{-0.24}$	$0.56(>0.06)$	0.02 (fix)	22.3/31
NGC 4374	$0.66^{+0.05}_{-0.04}$	$1.43(>0.26)$	$0.57(>0.17)$	$0.06^{+0.05}_{-0.06}$	71.6/59	$0.66^{+0.05}_{-0.05}$	$0.42^{+0.15}_{-0.09}$	$0.07^{+0.08}_{-0.07}$	71.5/60
NGC 4382	$0.35^{+0.09}_{-0.05}$	$0.74(>0.07)$	$1.01(>0.43)$	0.03 (fix)	37.3/29	$0.35^{+0.08}_{-0.05}$	$1.43^{+2.38}_{-0.90}$	0.03 (fix)	37.3/30
NGC 4406	$0.83^{+0.01}_{-0.01}$	$0.46^{+0.15}_{-0.14}$	$0.56^{+0.13}_{-0.08}$	$0.06^{+0.02}_{-0.02}$	246.0/143	$0.83^{+0.01}_{-0.01}$	$0.95^{+0.09}_{-0.06}$	$0.04^{+0.02}_{-0.02}$	261.2/144
NGC 4472	$0.96^{+0.01}_{-0.01}$	$0.40^{+0.08}_{-0.08}$	$0.58^{+0.08}_{-0.09}$	$0.07^{+0.01}_{-0.01}$	421.6/176	$0.98^{+0.01}_{-0.01}$	$1.04^{+0.05}_{-0.05}$	$0.04^{+0.01}_{-0.01}$	493.8/177
NGC 4552	$0.65^{+0.08}_{-0.06}$	$0.68(>0.08)$	$0.33(>0.12)$	0.03 (fix)	39.3/37	$0.64^{+0.06}_{-0.07}$	$0.42^{+0.22}_{-0.15}$	0.03 (fix)	39.4/38
NGC 4636	$0.75^{+0.01}_{-0.01}$	$0.54^{+0.07}_{-0.07}$	$0.50^{+0.03}_{-0.03}$	$0.04^{+0.01}_{-0.01}$	1093/372	$0.75^{+0.01}_{-0.01}$	$0.79^{+0.01}_{-0.01}$	$0.04^{+0.01}_{-0.01}$	1183/373
NGC 4649	$0.83^{+0.02}_{-0.01}$	$0.26^{+0.13}_{-0.08}$	$0.48^{+0.11}_{-0.10}$	$0.19^{+0.04}_{-0.05}$	217.9/114	$0.83^{+0.02}_{-0.02}$	$1.06^{+0.10}_{-0.08}$	$0.17^{+0.04}_{-0.04}$	250.2/115
NGC 4697	$0.35^{+0.05}_{-0.05}$	$0.88(>0.10)$	$0.76(>0.11)$	0.02 (fix)	36.6/31	$0.34^{+0.05}_{-0.04}$	$0.88^{+0.73}_{-0.41}$	0.02 (fix)	36.7/32
NGC 5018	$0.77^{+0.15}_{-0.19}$	$0.0 (>0.0)$	$3.2 (>0.01)$	0.07 (fix)	11.2/11	$0.77^{+0.15}_{-0.18}$	$28.3 (>0.02)$	0.07 (fix)	11.7/12
NGC 5846	$0.82^{+0.01}_{-0.01}$	$0.43^{+0.12}_{-0.05}$	$0.43^{+0.11}_{-0.04}$	$0.02^{+0.01}_{-0.01}$	213.0/120	$0.82^{+0.01}_{-0.01}$	$0.72^{+0.05}_{-0.05}$	$0.00^{+0.01}_{-0.00}$	230.7/121
NGC 7619	$0.81^{+0.03}_{-0.04}$	$0.44^{+0.33}_{-0.20}$	$0.46^{+0.33}_{-0.14}$	$0.19^{+0.10}_{-0.07}$	56.9/50	$0.80^{+0.03}_{-0.04}$	$0.83^{+0.27}_{-0.14}$	$0.22^{+0.12}_{-0.08}$	60.6/51
NGC 7626	$0.86^{+0.04}_{-0.04}$	$0.41(>0.05)$	$0.40(>0.20)$	0.06 (fix)	28.3/28	$0.86^{+0.03}_{-0.04}$	$0.72^{+0.30}_{-0.21}$	0.06 (fix)	29.1/29
IC 1459	$0.69^{+0.06}_{-0.07}$	$0.12^{+0.62}_{-0.12}$	$0.11^{+0.21}_{-0.05}$	0.01 (fix)	26.0/29	$0.68^{+0.06}_{-0.07}$	$0.41^{+0.22}_{-0.13}$	0.01 (fix)	29.6/30
IC 4296	$0.84^{+0.02}_{-0.03}$	$0.34^{+1.05}_{-0.24}$	$0.41^{+0.66}_{-0.15}$	0.04 (fix)	71.2/52	$0.83^{+0.02}_{-0.02}$	$0.81^{+0.24}_{-0.18}$	0.04 (fix)	72.8/53

Table 5.   Summary of spectral fits with MEKA, MEKAL and Masai codes.

galaxy	model	kT	A_α	A_{Fe}	N_H	χ^2/ν	kT	A_{Fe}	N_H	χ^2/ν
			varying A_α and A_{Fe}					A_α=1.0 solar (fixed)		
		(keV)	(solar)	(solar)	(10^{22} cm^{-2})					
NGC 499	MEKA	$0.59^{+0.02}_{-0.03}$	2.3(> 1.4)	2.4(> 1.5)	$0.18^{+0.05}_{-0.05}$	68.5/60	$0.60^{+0.02}_{-0.02}$	$1.14^{+0.19}_{-0.15}$	$0.14^{+0.05}_{-0.05}$	74.1/61
NGC 499	MEKAL	$0.64^{+0.02}_{-0.02}$	1.8(> 0.60)	1.9(> 0.76)	$0.23^{+0.07}_{-0.05}$	58.7/61	$0.64^{+0.02}_{-0.02}$	$1.15^{+0.24}_{-0.17}$	$0.22^{+0.06}_{-0.05}$	59.2/61
NGC 499	Masai	$0.73^{+0.02}_{-0.03}$	2.4 (> 1.6)	2.1 (> 1.6)	$0.11^{+0.06}_{-0.04}$	55.8/60	$0.73^{+0.02}_{-0.02}$	$1.47^{+0.25}_{-0.19}$	$0.10^{+0.05}_{-0.05}$	61.8/61
NGC 507	MEKA	$0.84^{+0.01}_{-0.02}$	$0.56^{+0.23}_{-0.18}$	$0.52^{+0.18}_{-0.11}$	$0.16^{+0.03}_{-0.02}$	236.3/112	$0.84^{+0.01}_{-0.02}$	$0.82^{+0.07}_{-0.08}$	$0.18^{+0.03}_{-0.04}$	245.2/113
NGC 507	MEKAL	$1.08^{+0.03}_{-0.03}$	$0.63^{+0.18}_{-0.19}$	$0.50^{+0.09}_{-0.11}$	$0.13^{+0.03}_{-0.03}$	148.0/112	$1.09^{+0.03}_{-0.03}$	$0.69^{+0.08}_{-0.06}$	$0.12^{+0.02}_{-0.02}$	157.0/113
NGC 507	Masai	$0.99^{+0.02}_{-0.02}$	$0.87^{+0.32}_{-0.27}$	$0.95^{+0.21}_{-0.26}$	$0.13^{+0.02}_{-0.03}$	206.1/112	$0.98^{+0.02}_{-0.02}$	$1.01^{+0.11}_{-0.09}$	$0.12^{+0.03}_{-0.02}$	206.2/113
NGC 720	MEKA	$0.49^{+0.03}_{-0.04}$	$0.25^{+0.26}_{-0.18}$	$0.21^{+0.13}_{-0.11}$	0.01 (fix)	28.2/31	$0.48^{+0.04}_{-0.04}$	$0.55^{+0.18}_{-0.12}$	0.01 (fix)	35.4/32
NGC 720	MEKAL	$0.54^{+0.04}_{-0.03}$	$0.12^{+0.21}_{-0.11}$	$0.21^{+0.13}_{-0.08}$	0.01 (fix)	30.7/31	$0.54^{+0.05}_{-0.06}$	$0.72^{+0.21}_{-0.16}$	0.01 (fix)	42.7/32
NGC 720	Masai	$0.54^{+0.04}_{-0.05}$	$0.27^{+0.27}_{-0.17}$	$0.22^{+0.13}_{-0.10}$	0.01 (fix)	30.0/31	$0.53^{+0.08}_{-0.06}$	$0.52^{+0.14}_{-0.11}$	0.01 (fix)	37.2/32
NGC 1316	MEKA	$0.59^{+0.02}_{-0.03}$	$0.43^{+0.66}_{-0.22}$	$0.36^{+0.40}_{-0.13}$	0.02 (fix)	68.7/66	$0.60^{+0.02}_{-0.04}$	$0.72^{+0.15}_{-0.14}$	0.02 (fix)	70.4/67
NGC 1316	MEKAL	$0.62^{+0.03}_{-0.05}$	$0.27^{+0.14}_{-0.15}$	$0.24^{+0.05}_{-0.07}$	$0.05^{+0.05}_{-0.04}$	67.9/66	$0.62^{+0.04}_{-0.04}$	$0.56^{+0.12}_{-0.05}$	$0.02^{+0.05}_{-0.02}$	74.9/67
NGC 1316	Masai	$0.71^{+0.04}_{-0.02}$	$0.47^{+0.34}_{-0.26}$	$0.52^{+0.22}_{-0.22}$	$0.00^{+0.02}_{-0.00}$	73.1/66	$0.70^{+0.04}_{-0.03}$	$0.77^{+0.24}_{-0.15}$	$0.00^{+0.01}_{-0.00}$	77.7/67
NGC 1332	MEKA	$0.44^{+0.04}_{-0.04}$	0.88(> 0.03)	0.55(> 0.06)	0.02 (fix)	29.6/20	$0.45^{+0.05}_{-0.04}$	$0.58^{+0.47}_{-0.21}$	0.02 (fix)	29.7/21
NGC 1332	MEKAL	$0.51^{+0.05}_{-0.07}$	0.95(> 0.0)	1.20(> 0.11)	0.02 (fix)	26.9/20	$0.52^{+0.04}_{-0.08}$	$1.20^{+1.22}_{-0.65}$	0.02 (fix)	27.0/21
NGC 1332	Masai	$0.48^{+0.06}_{-0.06}$	1.17(> 0.14)	0.68(> 0.09)	0.02 (fix)	29.6/20	$0.51^{+0.07}_{-0.06}$	$0.65^{+0.35}_{-0.24}$	0.02 (fix)	29.8/21
NGC 1399	MEKA	$0.86^{+0.01}_{-0.01}$	$0.23^{+0.07}_{-0.08}$	$0.45^{+0.07}_{-0.08}$	$0.14^{+0.02}_{-0.02}$	204.2/72	$0.85^{+0.01}_{-0.01}$	$1.05^{+0.09}_{-0.09}$	$0.13^{+0.02}_{-0.02}$	271.5/73
NGC 1399	MEKAL	$1.16^{+0.02}_{-0.02}$	$0.33^{+0.07}_{-0.12}$	$0.52^{+0.07}_{-0.02}$	$0.09^{+0.02}_{-0.02}$	184.2/72	$1.19^{+0.02}_{-0.02}$	$1.00^{+0.07}_{-0.07}$	$0.06^{+0.02}_{-0.02}$	230.3/73
NGC 1399	Masai	$1.02^{+0.01}_{-0.01}$	$0.35^{+0.13}_{-0.10}$	$0.75^{+0.15}_{-0.10}$	$0.10^{+0.01}_{-0.01}$	196.1/72	$1.01^{+0.02}_{-0.02}$	$1.33^{+0.08}_{-0.08}$	$0.08^{+0.01}_{-0.01}$	228.3/73
NGC 1404	MEKA	$0.52^{+0.01}_{-0.01}$	0.56(> 0.22)	$0.43^{+2.3}_{-0.20}$	$0.09^{+0.13}_{-0.02}$	55.6/41	$0.53^{+0.03}_{-0.07}$	$0.76^{+0.21}_{-0.07}$	$0.06^{+0.11}_{-0.06}$	55.9/42
NGC 1404	MEKAL	$0.60^{+0.03}_{-0.03}$	$0.36^{+0.48}_{-0.26}$	$0.41^{+0.31}_{-0.18}$	$0.06^{+0.05}_{-0.05}$	56.3/41	$0.60^{+0.03}_{-0.03}$	$0.85^{+0.16}_{-0.14}$	$0.05^{+0.04}_{-0.05}$	60.1/42
NGC 1404	Masai	$0.66^{+0.02}_{-0.02}$	$0.67^{+0.72}_{-0.43}$	$0.66^{+0.49}_{-0.27}$	$0.00^{+0.03}_{-0.00}$	62.0/41	$0.66^{+0.03}_{-0.03}$	$0.85^{+0.23}_{-0.14}$	$0.00^{+0.03}_{-0.00}$	63.3/42
NGC 1407	MEKA	$0.70^{+0.03}_{-0.02}$	$0.48^{+1.30}_{-0.22}$	$0.44^{+0.94}_{-0.14}$	$0.11^{+0.08}_{-0.05}$	83.4/63	$0.70^{+0.03}_{-0.02}$	$0.83^{+0.17}_{-0.18}$	$0.14^{+0.06}_{-0.07}$	84.4/64
NGC 1407	MEKAL	$0.87^{+0.06}_{-0.07}$	$0.28^{+0.13}_{-0.19}$	$0.26^{+0.08}_{-0.09}$	$0.08^{+0.09}_{-0.07}$	78.7/63	$0.82^{+0.05}_{-0.09}$	$0.55^{+0.29}_{-0.08}$	$0.12^{+0.18}_{-0.06}$	92.8/64
NGC 1407	Masai	$0.85^{+0.03}_{-0.03}$	$0.70^{+0.97}_{-0.40}$	$0.76^{+0.86}_{-0.29}$	$0.07^{+0.08}_{-0.05}$	77.6/63	$0.84^{+0.03}_{-0.03}$	$1.01^{+0.25}_{-0.13}$	$0.09^{+0.07}_{-0.06}$	78.3/64
NGC 3607	MEKA	$0.49^{+0.04}_{-0.04}$	0.25(> 0.0)	0.37(> 0.08)	0.02 (fix)	70.6/57	$0.49^{+0.04}_{-0.04}$	$1.09^{+0.95}_{-0.44}$	0.02 (fix)	71.2/58
NGC 3607	MEKAL	$0.53^{+0.04}_{-0.04}$	0.12(> 0.00)	0.29(> 0.13)	0.02 (fix)	68.3/57	$0.54^{+0.04}_{-0.04}$	$0.92^{+0.60}_{-0.37}$	0.02 (fix)	69.1/58
NGC 3607	Masai	$0.57^{+0.04}_{-0.06}$	1.16(> 0.03)	0.95(> 0.16)	0.02 (fix)	65.8/57	$0.57^{+0.05}_{-0.05}$	$0.86^{+0.45}_{-0.22}$	0.02 (fix)	66.2/58
NGC 3923	MEKA	$0.55^{+0.05}_{-0.06}$	0.31(> 0.0)	0.26(> 0.07)	0.06 (fix)	30.2/26	$0.55^{+0.05}_{-0.06}$	$0.59^{+0.47}_{-0.29}$	0.06 (fix)	30.6/27
NGC 3923	MEKAL	$0.61^{+0.06}_{-0.08}$	0.07(> 0.0)	0.15(> 0.08)	0.06 (fix)	30.6/26	$0.61^{+0.06}_{-0.07}$	$0.61^{+0.32}_{-0.20}$	0.06 (fix)	32.1/27
NGC 3923	Masai	$0.67^{+0.06}_{-0.07}$	0.56 (> 0.0)	0.59(> 0.09)	0.06 (fix)	32.2/26	$0.67^{+0.06}_{-0.06}$	$0.84^{+0.60}_{-0.50}$	0.06 (fix)	32.6/27
NGC 4125	MEKA	$0.43^{+0.05}_{-0.04}$	0.80 (> 0.22)	0.49(> 0.18)	0.02 (fix)	21.8/24	$0.42^{+0.05}_{-0.04}$	$0.60^{+0.38}_{-0.19}$	0.02 (fix)	22.0/25
NGC 4125	MEKAL	$0.45^{+0.07}_{-0.06}$	1.28(> 0.16)	1.11 (> 0.26)	0.02 (fix)	22.2/24	$0.45^{+0.06}_{-0.06}$	$1.01^{+0.73}_{-0.35}$	0.02 (fix)	22.2/25
NGC 4125	Masai	$0.44^{+0.05}_{-0.05}$	1.46 (> 0.34)	0.76(> 0.26)	0.02 (fix)	19.9/24	$0.44^{+0.05}_{-0.05}$	$0.60^{+0.33}_{-0.17}$	0.02 (fix)	20.1/25
NGC 4365	MEKA	$0.43^{+0.19}_{-0.21}$	0.0(> 0.0)	0.05 (>0.0)	0.03 (fix)	21.4/31	$0.35^{+0.23}_{-0.15}$	0.46 (> 0.06)	0.03 (fix)	21.6/31
NGC 4365	MEKAL	$0.52^{+0.22}_{-0.28}$	0.00 (> 0.0)	0.09 (> 0.0)	0.02 (fix)	21.7/31	$0.33^{+0.40}_{-0.15}$	0.60(> 0.04)	0.02 (fix)	22.2/30
NGC 4365	Masai	$0.47^{+0.25}_{-0.25}$	0.0 (> 0.0)	0.04(> 0.0)	0.02 (fix)	21.3/30	$0.42^{+0.32}_{-0.20}$	$0.44^{+3.60}_{-0.38}$	0.02 (fix)	21.8/30
NGC 4374	MEKA	$0.54^{+0.05}_{-0.07}$	1.2(> 0.29)	0.64(> 0.19)	$0.12^{+0.08}_{-0.08}$	72.8/59	$0.54^{+0.05}_{-0.07}$	$0.57^{+0.25}_{-0.18}$	$0.12^{+0.09}_{-0.09}$	72.8/60
NGC 4374	MEKAL	$0.60^{+0.05}_{-0.05}$	0.94(> 0.42)	0.54(> 0.25)	$0.10^{+0.05}_{-0.07}$	78.0/59	$0.60^{+0.05}_{-0.05}$	$0.57^{+0.19}_{-0.13}$	$0.10^{+0.07}_{-0.06}$	78.0/60
NGC 4374	Masai	$0.66^{+0.05}_{-0.06}$	1.65 (> 0.51)	0.94(> 0.37)	$0.05^{+0.07}_{-0.05}$	68.8/59	$0.67^{+0.06}_{-0.08}$	$0.65^{+0.25}_{-0.21}$	$0.05^{+0.07}_{-0.05}$	69.3/60

Table 5. (continued)

galaxy	model	A_α , $A_{\rm Fe}$ free parameter					A_α=1.0 solar (fixed)			
		kT	A_α	$A_{\rm Fe}$	N_H	χ^2/ν	kT	$A_{\rm Fe}$	N_H	χ^2/ν
		(keV)	(solar)	(solar)	$(10^{22}\,{\rm cm}^{-2})$					
NGC 4382	MEKA	$0.32^{+0.04}_{-0.05}$	19.3 (> 0.02)	26.9 (> 0.15)	0.03 (fix)	38.9/29	$0.32^{+0.05}_{-0.04}$	1.46(> 0.68)	0.03 (fix)	39.0/30
NGC 4382	MEKAL	$0.29^{+0.09}_{-0.06}$	0.33 (> 0.0)	1.9 (> 0.30)	0.03 (fix)	37.2/29	$0.29^{+0.09}_{-0.07}$	6.14(> 0.62)	0.03 (fix)	37.3/30
NGC 4382	Masai	$0.35^{+0.05}_{-0.05}$	2.5 (> 0.08)	3.4 (> 0.15)	0.03 (fix)	36.5/29	$0.35^{+0.06}_{-0.05}$	$1.44^{+3.05}_{-0.90}$	0.03 (fix)	36.5/30
NGC 4406	MEKA	$0.65^{+0.01}_{-0.01}$	$1.02^{+0.88}_{-0.37}$	$1.12^{+0.85}_{-0.35}$	$0.09^{+0.01}_{-0.01}$	276.4/143	$0.65^{+0.01}_{-0.01}$	$1.13^{+0.06}_{-0.06}$	$0.09^{+0.02}_{-0.02}$	276.5/144
NGC 4406	MEKAL	$0.72^{+0.01}_{-0.01}$	$0.45^{+0.18}_{-0.08}$	$0.48^{+0.13}_{-0.06}$	$0.12^{+0.03}_{-0.02}$	243.0/143	$0.72^{+0.01}_{-0.02}$	$0.82^{+0.07}_{-0.05}$	$0.12^{+0.03}_{-0.02}$	258.1/144
NGC 4406	Masai	$0.79^{+0.01}_{-0.01}$	$1.13^{+0.68}_{-0.32}$	$1.45^{+0.81}_{-0.23}$	$0.02^{+0.02}_{-0.01}$	254.0/143	$0.79^{+0.01}_{-0.01}$	$1.30^{+0.10}_{-0.07}$	$0.03^{+0.02}_{-0.01}$	254.4/144
NGC 4472	MEKA	$0.74^{+0.01}_{-0.01}$	$0.36^{+0.06}_{-0.06}$	$0.49^{+0.06}_{-0.06}$	$0.11^{+0.02}_{-0.02}$	806.6/176	$0.74^{+0.01}_{-0.01}$	$1.04^{+0.05}_{-0.05}$	$0.10^{+0.02}_{-0.02}$	863.6/177
NGC 4472	MEKAL	$0.93^{+0.01}_{-0.01}$	$0.31^{+0.06}_{-0.05}$	$0.38^{+0.04}_{-0.05}$	$0.08^{+0.01}_{-0.01}$	604.2/176	$0.94^{+0.01}_{-0.01}$	$0.74^{+0.03}_{-0.04}$	$0.06^{+0.02}_{-0.02}$	747.7/177
NGC 4472	Masai	$0.89^{+0.01}_{-0.01}$	$0.58^{+0.08}_{-0.08}$	$0.87^{+0.10}_{-0.10}$	$0.06^{+0.02}_{-0.02}$	697.1/176	$0.89^{+0.01}_{-0.01}$	$1.24^{+0.12}_{-0.12}$	$0.06^{+0.02}_{-0.02}$	717.9/177
NGC 4552	MEKA	$0.55^{+0.05}_{-0.05}$	0.64(> 0.13)	0.41(> 0.17)	0.03 (fix)	38.6/37	$0.55^{+0.05}_{-0.05}$	$0.61^{+0.41}_{-0.24}$	0.03 (fix)	38.6/38
NGC 4552	MEKAL	$0.60^{+0.06}_{-0.06}$	0.54(> 0.07)	0.36(> 0.16)	0.03 (fix)	39.7/37	$0.60^{+0.05}_{-0.06}$	$0.61^{+0.31}_{-0.22}$	0.03 (fix)	39.8/38
NGC 4552	Masai	$0.64^{+0.07}_{-0.10}$	0.90(> 0.11)	0.57(> 0.19)	0.03 (fix)	38.8/37	$0.63^{+0.07}_{-0.09}$	$0.61^{+0.44}_{-0.27}$	0.03 (fix)	38.8/38
NGC 4636	MEKA	$0.59^{+0.01}_{-0.01}$	$1.66^{+1.8}_{-0.08}$	$1.56^{+1.8}_{-0.10}$	$0.09^{+0.01}_{-0.01}$	1235/372	$0.59^{+0.01}_{-0.01}$	$0.97^{+0.03}_{-0.03}$	$0.08^{+0.01}_{-0.01}$	1272/373
NGC 4636	MEKAL	$0.65^{+0.01}_{-0.01}$	$0.74^{+0.13}_{-0.08}$	$0.71^{+0.07}_{-0.06}$	$0.11^{+0.01}_{-0.01}$	728.4/372	$0.66^{+0.01}_{-0.01}$	$0.89^{+0.01}_{-0.02}$	$0.10^{+0.01}_{-0.01}$	753.5/373
NGC 4636	Masai	$0.74^{+0.01}_{-0.01}$	$1.60^{+0.35}_{-0.18}$	$1.68^{+0.24}_{-0.14}$	$0.02^{+0.01}_{-0.01}$	785.8/372	$0.74^{+0.01}_{-0.01}$	$1.24^{+0.03}_{-0.03}$	$0.02^{+0.01}_{-0.01}$	822.6/373
NGC 4649	MEKA	$0.66^{+0.02}_{-0.02}$	$0.54^{+0.42}_{-0.14}$	$0.70^{+0.40}_{-0.14}$	$0.18^{+0.02}_{-0.03}$	236.5/114	$0.66^{+0.02}_{-0.02}$	$1.10^{+0.14}_{-0.14}$	$0.18^{+0.04}_{-0.04}$	239.4/115
NGC 4649	MEKAL	$0.74^{+0.02}_{-0.03}$	$0.26^{+0.18}_{-0.06}$	$0.41^{+0.17}_{-0.06}$	$0.24^{+0.07}_{-0.04}$	207.2/114	$0.72^{+0.02}_{-0.03}$	$1.09^{+0.28}_{-0.15}$	$0.30^{+0.10}_{-0.09}$	228.2/115
NGC 4649	Masai	$0.81^{+0.01}_{-0.01}$	$0.68^{+0.33}_{-0.27}$	$1.04^{+0.40}_{-0.22}$	$0.12^{+0.03}_{-0.03}$	217.8/114	$0.81^{+0.01}_{-0.01}$	$1.41^{+0.16}_{-0.17}$	$0.13^{+0.03}_{-0.04}$	220.4/115
NGC 4697	MEKA	$0.33^{+0.04}_{-0.04}$	1.1 (> 0.11)	0.74 (> 0.10)	0.02 (fix)	36.0/31	$0.33^{+0.04}_{-0.03}$	$0.70^{+0.51}_{-0.30}$	0.02 (fix)	36.3/32
NGC 4697	MEKAL	$0.31^{+0.05}_{-0.05}$	1.6 (> 0.08)	2.9(> 0.22)	0.02 (fix)	39.3/31	$0.31^{+0.05}_{-0.05}$	$1.85^{+2.31}_{-1.13}$	0.02 (fix)	39.4/32
NGC 4697	Masai	$0.34^{+0.05}_{-0.04}$	1.8 (> 0.12)	1.4(> 0.13)	0.02 (fix)	34.7/31	$0.35^{+0.05}_{-0.05}$	$0.83^{+1.35}_{-0.52}$	0.02 (fix)	34.7/32
NGC 5018	MEKA	$0.63^{+0.12}_{-0.15}$	0.0 (> 0.0)	5.3 (> 0.05)	0.07 (fix)	13.3/11	$0.63^{+0.12}_{-0.15}$	2.2 (> 0.0)	0.07 (fix)	13.3/12
NGC 5018	MEKAL	$0.71^{+0.21}_{-0.20}$	0.0 (> 0.0)	1.7(> 0.10)	0.07 (fix)	10.9/11	$0.72^{+0.19}_{-0.19}$	34.7(> 0.0)	0.07 (fix)	10.9/12
NGC 5018	Masai	$0.76^{+0.15}_{-0.33}$	0.0 (> 0.0)	3.3(> 0.12)	0.07 (fix)	11.6/11	$0.76^{+0.14}_{-0.26}$	4.6(> 0.0)	0.07 (fix)	11.6/12
NGC 5846	MEKA	$0.65^{+0.01}_{-0.01}$	$0.87^{+0.34}_{-0.33}$	$0.79^{+0.21}_{-0.23}$	$0.05^{+0.02}_{-0.02}$	230.0/120	$0.65^{+0.01}_{-0.01}$	$0.87^{+0.06}_{-0.07}$	$0.05^{+0.02}_{-0.02}$	247.6/121
NGC 5846	MEKAL	$0.71^{+0.01}_{-0.01}$	$0.42^{+0.10}_{-0.11}$	$0.36^{+0.08}_{-0.05}$	$0.07^{+0.02}_{-0.02}$	225.3/120	$0.68^{+0.02}_{-0.02}$	$0.69^{+0.06}_{-0.06}$	$0.10^{+0.03}_{-0.02}$	253.4/121
NGC 5846	Masai	$0.79^{+0.01}_{-0.01}$	$0.98^{+0.28}_{-0.24}$	$1.07^{+0.25}_{-0.19}$	$0.00^{+0.01}_{-0.00}$	204.0/121	$0.79^{+0.01}_{-0.01}$	$1.10^{+0.08}_{-0.07}$	$0.00^{+0.01}_{-0.00}$	204.1/121
NGC 7619	MEKA	$0.64^{+0.02}_{-0.04}$	1.56 (> 0.65)	1.21(> 0.56)	$0.22^{+0.04}_{-0.08}$	75.1/50	$0.63^{+0.03}_{-0.02}$	$0.83^{+0.12}_{-0.14}$	$0.21^{+0.04}_{-0.08}$	75.9/51
NGC 7619	MEKAL	$0.70^{+0.05}_{-0.04}$	$0.61^{+0.81}_{-0.31}$	$0.56^{+0.64}_{-0.24}$	$0.26^{+0.11}_{-0.09}$	48.2/50	$0.69^{+0.04}_{-0.04}$	$0.85^{+0.24}_{-0.09}$	$0.30^{+0.10}_{-0.09}$	49.4/51
NGC 7619	Masai	$0.78^{+0.01}_{-0.02}$	1.52 (> 0.71)	1.48(> 0.81)	$0.15^{+0.06}_{-0.06}$	59.1/50	$0.78^{+0.03}_{-0.02}$	$1.08^{+0.16}_{-0.16}$	$0.15^{+0.05}_{-0.06}$	59.9/51
NGC 7626	MEKA	$0.69^{+0.04}_{-0.04}$	0.77(> 0.14)	0.63(> 0.24)	0.06 (fix)	35.0/28	$0.69^{+0.04}_{-0.04}$	$0.78^{+0.39}_{-0.23}$	0.06 (fix)	35.1/29
NGC 7626	MEKAL	$0.83^{+0.07}_{-0.08}$	$0.44^{+1.06}_{-0.42}$	$0.29^{+0.50}_{-0.15}$	0.06 (fix)	33.8/28	$0.81^{+0.07}_{-0.07}$	$0.56^{+0.22}_{-0.16}$	0.06 (fix)	35.4/29
NGC 7626	Masai	$0.82^{+0.04}_{-0.04}$	1.46 (> 0.29)	1.37(> 0.47)	0.06 (fix)	31.2/28	$0.84^{+0.04}_{-0.04}$	$1.06^{+0.44}_{-0.33}$	0.06 (fix)	31.2/29
IC 1459	MEKA	$0.57^{+0.05}_{-0.05}$	$0.12^{+1.05}_{-0.12}$	$0.13^{+0.64}_{-0.05}$	0.01 (fix)	31.4/29	$0.57^{+0.05}_{-0.05}$	$0.63^{+0.40}_{-0.23}$	0.01 (fix)	33.8/30
IC 1459	MEKAL	$0.63^{+0.06}_{-0.05}$	$0.12^{+0.59}_{-0.12}$	$0.13^{+0.31}_{-0.06}$	0.01 (fix)	28.0/29	$0.63^{+0.05}_{-0.06}$	$0.55^{+0.32}_{-0.18}$	0.01 (fix)	31.5/30
IC 1459	Masai	$0.66^{+0.07}_{-0.08}$	$0.25^{+1.43}_{-0.24}$	$0.20^{+0.68}_{-0.12}$	0.01 (fix)	27.1/29	$0.66^{+0.06}_{-0.07}$	$0.55^{+0.34}_{-0.19}$	0.01 (fix)	28.7/30
IC 4296	MEKA	$0.66^{+0.02}_{-0.03}$	1.09 (> 0.20)	1.06 (> 0.30)	0.05 (fix)	82.6/52	$0.66^{+0.02}_{-0.02}$	$0.95^{+0.34}_{-0.25}$	0.04 (fix)	82.6/53
IC 4296	MEKAL	$0.76^{+0.04}_{-0.04}$	$0.35^{+0.83}_{-0.26}$	$0.33^{+0.42}_{-0.15}$	0.04 (fix)	79.6/52	$0.75^{+0.04}_{-0.04}$	$0.64^{+0.17}_{-0.13}$	0.04 (fix)	81.7/53
IC 4296	Masai	$0.79^{+0.03}_{-0.03}$	1.2 (> 0.32)	1.34(> 0.59)	0.04 (fix)	82.9/52	$0.80^{+0.03}_{-0.03}$	$1.15^{+0.35}_{-0.25}$	0.04 (fix)	82.9/53

Table 6. Temperature (keV) and χ^2 derived from fitting the spectra above 1.6 keV (SIS) and 1.7 keV (GIS) with vR-S model.

	temperature (keV)	χ^2/dof.
NGC 507	1.05±0.12	49.2/42
NGC 1399	1.06±0.10	47.2/28
NGC 4406	0.80±0.11	57.6/52
NGC 4472	1.05±0.07	116.9/81
NGC 4636	0.73±0.04	210.6/202
NGC 5846	0.80±0.12	42.4/37

Table 7. The fitting results for the SIS spectra by adding 20 % systematic errors in 0.4-1.6 keV. The Raymond-Smith model has been used.

galaxy	model	kT (keV)	A_α (solar)	$A_{\rm Fe}$ (solar)	N_H (10^{22}cm^{-2})	χ^2/ν
NGC 507	R-S	$1.02^{+0.04}_{-0.08}$	$0.48^{+0.30}_{-0.16}$	$0.43^{+0.27}_{-0.15}$	$0.16^{+0.08}_{-0.04}$	77/101
NGC 507	MEKA	$0.87^{+0.06}_{-0.04}$	$0.44^{+0.22}_{-0.14}$	$0.44^{+0.16}_{-0.14}$	$0.21^{+0.04}_{-0.10}$	94/101
NGC 507	MEKAL	$1.02^{+0.08}_{-0.06}$	$0.52^{+0.28}_{-0.16}$	$0.39^{+0.18}_{-0.12}$	$0.18^{+0.04}_{-0.06}$	72/101
NGC 507	Masai	$0.97^{+0.06}_{-0.05}$	$0.57^{+0.34}_{-0.16}$	$0.63^{+0.30}_{-0.19}$	$0.18^{+0.04}_{-0.06}$	87/101
NGC 1399	R-S	$1.09^{+0.04}_{-0.03}$	$0.51^{+0.16}_{-0.16}$	$0.72^{+0.24}_{-0.18}$	$0.10^{+0.04}_{-0.04}$	96/83
NGC 1399	MEKA	$0.94^{+0.05}_{-0.06}$	$0.37^{+0.12}_{-0.12}$	$0.56^{+0.15}_{-0.15}$	$0.14^{+0.04}_{-0.04}$	100/83
NGC 1399	MEKAL	$1.12^{+0.07}_{-0.07}$	$0.49^{+0.17}_{-0.16}$	$0.53^{+0.22}_{-0.13}$	$0.10^{+0.04}_{-0.03}$	96/83
NGC 1399	Masai	$1.04^{+0.05}_{-0.04}$	$0.49^{+0.23}_{-0.12}$	$0.91^{+0.32}_{-0.16}$	$0.12^{+0.03}_{-0.04}$	91/83
NGC 4406	R-S	$0.83^{+0.03}_{-0.05}$	$0.86^{+0.66}_{-0.41}$	$0.88^{+0.57}_{-0.13}$	$0.04^{+0.06}_{-0.04}$	69/118
NGC 4406	MEKA	$0.64^{+0.05}_{-0.05}$	$0.72^{+1.43}_{-0.27}$	$0.77^{+1.23}_{-0.25}$	$0.11^{+0.06}_{-0.06}$	80/118
NGC 4406	MEKAL	$0.74^{+0.06}_{-0.05}$	$0.63^{+0.68}_{-0.23}$	$0.68^{+0.49}_{-0.20}$	$0.10^{+0.06}_{-0.06}$	71/118
NGC 4406	Masai	$0.79^{+0.03}_{-0.05}$	$0.93^{+1.53}_{-0.33}$	$1.21^{+1.53}_{-0.36}$	$0.05^{+0.06}_{-0.05}$	67/118
NGC 4472	R-S	$1.00^{+0.06}_{-0.03}$	$0.77^{+0.23}_{-0.23}$	$0.94^{+0.23}_{-0.22}$	$0.06^{+0.03}_{-0.03}$	156/157
NGC 4472	MEKA	$0.86^{+0.04}_{-0.03}$	$0.54^{+0.16}_{-0.15}$	$0.74^{+0.10}_{-0.21}$	$0.11^{+0.03}_{-0.05}$	202/157
NGC 4472	MEKAL	$1.02^{+0.04}_{-0.06}$	$0.79^{+0.21}_{-0.25}$	$0.75^{+0.13}_{-0.18}$	$0.07^{+0.03}_{-0.03}$	156/157
NGC 4472	Masai	$0.95^{+0.04}_{-0.05}$	$0.65^{+0.35}_{-0.10}$	$0.94^{+0.44}_{-0.16}$	$0.08^{+0.03}_{-0.04}$	165/157
NGC 4636	R-S	$0.76^{+0.02}_{-0.02}$	$0.95^{+0.25}_{-0.15}$	$0.75^{+0.13}_{-0.09}$	$0.01^{+0.03}_{-0.01}$	223/330
NGC 4636	MEKA	$0.63^{+0.02}_{-0.02}$	$1.10^{+0.44}_{-0.21}$	$1.12^{+0.37}_{-0.20}$	$0.06^{+0.01}_{-0.02}$	337/330
NGC 4636	MEKAL	$0.72^{+0.01}_{-0.02}$	$1.13^{+0.16}_{-0.19}$	$0.88^{+0.10}_{-0.13}$	$0.04^{+0.03}_{-0.03}$	247/330
NGC 4636	Masai	$0.72^{+0.02}_{-0.02}$	$1.17^{+0.25}_{-0.20}$	$1.33^{+0.30}_{-0.23}$	$0.02^{+0.02}_{-0.02}$	272/330
NGC 5846	R-S	$0.81^{+0.03}_{-0.04}$	$0.70^{+0.37}_{-0.21}$	$0.57^{+0.26}_{-0.16}$	$0.00^{+0.05}_{-0.00}$	98.1/103
NGC 5846	MEKA	$0.64^{+0.05}_{-0.03}$	$0.77^{+0.37}_{-0.21}$	$0.67^{+0.26}_{-0.16}$	$0.07^{+0.05}_{-0.00}$	96.8/103
NGC 5846	MEKAL	$0.72^{+0.05}_{-0.05}$	$0.68^{+0.40}_{-0.16}$	$0.53^{+0.30}_{-0.13}$	$0.04^{+0.05}_{-0.04}$	93/103
NGC 5846	Masai	$0.77^{+0.03}_{-0.03}$	$1.22^{+0.84}_{-0.47}$	$1.22^{+0.72}_{-0.39}$	$0.00^{+0.03}_{-0.04}$	83/103

Table 8.   The results from combined fit to spectra of galaxies with similar ISM luminosity and temperature.

	Model	A_α	$A_{\rm Fe}$	χ^2/bin
Group1	R-S	$0.62^{+0.17}_{-0.19}$	$0.69^{+0.17}_{-0.19}$	453.7/397
	MEKAL	$0.66^{+0.15}_{-0.16}$	$0.61^{+0.10}_{-0.10}$	483.4/397
	MEKA	$0.50^{+0.22}_{-0.13}$	$0.53^{+0.18}_{-0.11}$	606.9/397
	Masai	$0.72^{+0.21}_{-0.13}$	$0.88^{+0.12}_{-0.10}$	498.7/397
Group2	R-S	$0.69^{+0.23}_{-0.24}$	$0.60^{+0.22}_{-0.20}$	370.2/379
	MEKAL	$0.77^{+0.21}_{-0.29}$	$0.64^{+0.19}_{-0.22}$	360.8/379
	MEKA	$1.01^{+0.53}_{-0.20}$	$0.80^{+0.30}_{-0.15}$	411.1/379
	Masai	$1.10^{+0.53}_{-0.23}$	$1.22^{+0.40}_{-0.19}$	351.1/379
Group3	R-S	$0.38^{+0.45}_{-0.10}$	$0.47^{+0.44}_{-0.08}$	204.2/217
	MEKAL	$0.55^{+0.36}_{-0.25}$	$0.59^{+0.22}_{-0.20}$	203.1/217
	MEKA	$0.80^{+0.38}_{-0.30}$	$0.77^{+0.26}_{-0.22}$	256.2/217
	Masai	$1.00^{+0.66}_{-0.40}$	$1.20^{+0.50}_{-0.42}$	224.8/217
Group4	R-S	$1.00^{+0.20}_{-0.20}$	$0.78^{+0.10}_{-0.12}$	422.6/453
	MEKAL	$1.00^{+0.30}_{-0.10}$	$0.90^{+0.10}_{-0.10}$	477.5/453
	MEKA	$1.15^{+0.35}_{-0.21}$	$1.13^{+0.33}_{-0.18}$	685.8/453
	Masai	$1.18^{+0.25}_{-0.22}$	$1.34^{+0.30}_{-0.25}$	508.0/453
Group5	R-S	$0.47^{+0.33}_{-0.35}$	$0.27^{+0.12}_{-0.16}$	255.8/229
	MEKAL	$0.42^{+0.37}_{-0.27}$	$0.32^{+0.19}_{-0.14}$	249.8/229
	MEKA	$0.58^{+0.32}_{-0.43}$	$0.48^{+0.14}_{-0.28}$	247.1/229
	Masai	$0.74^{+0.40}_{-0.35}$	$0.60^{+0.20}_{-0.25}$	247.6/229
Group6	R-S	$0.30^{+0.70}_{-0.18}$	$0.18^{+0.27}_{-0.07}$	139.0/147
	MEKAL	$0.21^{+0.73}_{-0.13}$	$0.17^{+0.30}_{-0.10}$	132.0/147
	MEKA	$0.21^{+0.68}_{-0.13}$	$0.17^{+0.32}_{-0.09}$	132.0/147
	Masai	$0.36^{+0.65}_{-0.22}$	$0.26^{+0.30}_{-0.13}$	130.2/147

	kT	L_X	member
Group1	> 0.9 keV	$> 10^{41}{\rm ergs}^{-1}$	NGC 507, NGC 1399, & NGC 4472
Group2	$0.8 \sim 0.9$ keV	$> 10^{41}{\rm ergs}^{-1}$	NGC 4406, NGC 5846, NGC 7619, & IC 4296
Group3	$0.8 \sim 0.9$ keV	$5 \times 10^{40} \sim 10^{41}{\rm ergs}^{-1}$	NGC 1407, NGC 4649 & NGC 7626
Group4	$0.6 \sim 0.8$ keV	$> 10^{41}{\rm ergs}^{-1}$	NGC 4636, & NGC 499
Group5	$0.6 \sim 0.8$ keV	$< 5 \times 10^{40}{\rm ergs}^{-1}$	NGC 1332, NGC 1404, NGC 4552, NGC 3923, NGC 4374, IC 1459, NGC 5018, & NGC 1316
Group6	$0.4 \sim 0.6$ keV	$< 5 \times 10^{40}{\rm ergs}^{-1}$	NGC 720, NGC 4125, NGC 4365 & NGC 3607